공학박사학위논문

Analysis of abnormal grain growth and improvement in grain-oriented electrical steel based on solid-state wetting mechanism

고상 젖음 이론을 바탕으로 접근한 비정상 입자 성장 분석과 전기강판의 개선

2016년 8월

서울대학교 대학원

재료공학부

나 태 욱

ABSTRACT

Analysis of abnormal grain growth and improvement in grain-oriented electrical steel based on solid-state wetting mechanism

Tae-Wook Na

Department of Materials Science and Engineering

The Graduate School

Seoul National University

Abnormal grain growth(AGG) occurs frequently in many metallic systems. One of the famous examples is the Goss grain which abnormally grows during secondary recrystallization in Fe-3%Si steel. This phenomenon is already used for the grain-oriented electrical steel but its mechanism has not been clearly understood.

The sub-boundary enhanced solid-state wetting has been suggested to explain the mechanism of AGG. This theory suggests that the sub-boundary increases the wetting probability and the increased wetting probability enhances AGG. In this

paper, based on this theory, microstructure and morphology of abnormally growing grains and matrix grains are analyzed and the grain-oriented electrical steel is improved.

At the first, misorientation measurements at the growth front of abnormally growing grains in 5052 aluminum alloy were made using electron back-scattered diffraction (EBSD). When a three-dimensional morphology of solid-state wetting along a triple junction line is observed on a two-dimensional section, two kinds of morphologies could be observed. One is a morphology of penetrating the grain boundary when the section is parallel to the triple junction line. Grain boundary energies, which were estimated from misorientation measurements of the three grains in the penetrating morphology, satisfied the energetic condition for wetting along the triple junction line. Misorientation measurements showed that some matrix grains away from the growth front of abnormally growing grains had the same crystallographic orientation as that of the abnormally growing grain. This result implies that the abnormal grain growth in 5052 aluminum alloy occurs by the mechanism of sub-boundary enhanced solid-state wetting.

The morphology of abnormally growing grains are predicted by three-dimensional Monte Carlo simulation and the real three-dimensional morphology is reconstructed by serial sectioning. The simulation was performed with sub-boundaries, precipitates and real crystallographic orientations of matrix grains. In the simulation, AGG occurs only when the both of sub-boundaries and precipitates

exist. Form this simulation result, AGG occurs based on sub-boundary enhanced solid-state wetting mechanism. The real three-dimensional morphologies of abnormally growing grains are extremely similar to that of simulated abnormally growing grains. Both grains have island, peninsular grains and extremely irregular shape. This result shows that the factors are applied realistically in the simulation. Because the simulation shows realistic AGG, the behavior of abnormal grain growth was analyzed by the simulation. The simulation shows that the sub-boundary energy and the crystallographic orientation of matrix grains determine the velocity of AGG.

According the analysis, the rate of AGG is determined by texture of matrix grains. And the texture can be controlled by asymmetric rolling. By the asymmetric rolling, the AGG rate are fastened and the magnetic properties of the grain-oriented electrical steel is improved.

Keywords: Abnormal grain growth; Solid-state wetting; Sub-boundary; Grain boundary energy; Three-dimensional morphology; Monte-Carlo simulation; Serial sectioning; Asymmetric rolling

Student Number: 2010-20599

Contents

LIST OF FIGURES

simulation microstructure at z = 40 after 13000, 13300, 13600 and 14000 MCS.

Figure 8.13 (a), (c) Two-dimensional microstructures of NGG and AGG and (b), (d) three-dimensional morphologies of Goss grain growing by NGG and AGG, respectively.

CHAPTER 1

Introduction

1.1 Abnormal grain growth in metallic system

There are two types of grain growth; normal grain growth (NGG) and abnormal grain growth (AGG) [1]. The grain size increases homogeneously and gradually during NGG; the grain size dispersion does not change. The grains grow reduces the grain boundary area and, hence, reduce the total grain boundary energy. When finely dispersed precipitates or a strong texture inhibit NGG, AGG referred to as secondary recrystallization occurs. When AGG occurs, only a few grains grow abnormally consuming the neighboring matrix grains, which results in the binary grain size distribution; large abnormally grown grains and small retained matrix grains.

AGG occurs in many metallic systems [2-6]. For example, in Fe-3%Si steel Goss grains with {110}<001> crystallographic orientation undergo AGG exclusively [7]. The selective AGG results in a strong Goss texture, which has an advantage of decreasing the magnetization energy loss of transformer cores. Because of the scientific and technological interests, the mechanism of the Goss texture formation has been studied extensively since Goss [7] reported this phenomenon in 1935.

Previously, the AGG mechanism was approached mainly from the viewpoint that the grain boundaries of abnormally growing grains have the high migration rate compared with those of the non-abnormally growing grains. It was suggested that the high migration rate was made by the high mobility or by less pinning of the grain boundary. For example, Harase et al. [8] and Ushigami et al. [9] proposed that Goss grains have the higher fraction of a coincidence site lattice (CSL) grain boundary than other matrix grains and the CSL grain boundaries have the higher mobility than other grain boundaries. On the other hand, Homma et al. [10] proposed that Goss grains have a higher fraction of Σ9 grain boundaries than other matrix grains. Further, they proposed that the Σ9 grain boundaries have the higher migration velocity because they have low energy and thereby can overcome Zener pinning more easily than other grain boundaries. In contrast with the suggestion that Goss grains have a higher fraction of CSL boundaries including Σ9 than other grains, Szpunar et al. [11] reported based on their misorientation measurements by electron back scattered diffraction (EBSD) that Goss grains do not have a higher fraction of CSL boundaries than other matrix grains but have a higher fraction of middle orientation boundaries with misorientation angles between 20° and 45°. From this result, they proposed that middle orientation grain boundaries have a high migration rate, playing a key role in AGG. However, these theories have drawbacks and received criticisms. For example, Morawiec et al. [12] reported that it is not sufficient to explain the growth advantage of the Goss grain based on only misorientations of grain boundaries because non-Goss grains in primary matrix grains also have CSL grain boundaries, especially Σ9 boundary, and 20-45° misorientation grain boundaries whose frequency is not less than that of the Goss grain. Besides, based on misorientation measurements, Etter et al. [13] suggested that the Goss grain didn’t have a higher percentage of CSL relationship with matrix grains than other-oriented grains and that the middle misorientation boundaries with the angle in the range of 20-45° have the highest percentage of not only disappearing grains but also remaining grains during secondary recrystallization, which means that the middle misorientation boundaries do not have a high mobility.

1.2 Solid-state wetting

Driving force of grain growth is the decrease of grain boundary energy because there is not the bulk energy difference among the recrystallized grains. One way to decrease the grain boundary energy is to decrease the grain boundary area. If there is a curved grain boundary and it is flattened, the grain boundary area is decrease. So the grain boundary curvature can be the driving force of grain growth. The force balance of the grain boundary energy at the triple junction makes grain boundary curvature. As a result, the force balance at the triple junction makes grain boundary curvature and the curvature is the driving force of grain growth.

Gottstein et al. [14, 15] suggested that the triple-junction line mobility plays a more dominant role than the grain boundary mobility in the grain growth. The role of triple-junction line mobility becomes clear if we consider that the growing grain should have negative or inward curvatures, whose geometrical condition is satisfied only when the triple junction line goes ahead of the grain boundary.

Figure 1.1 is the Schematics of grain boundary migration when the triple junctions are fixed and moved. The grain boundary migration is driven by grain boundary curvature. The grain boundary C in figure 1.1(a) has curvature so the grain boundary C will migrate toward grain B. If the velocity of triple junction is slow and the grain boundary migration rate is fast, then the grain boundary migration occurs until the grain boundary curvature exists. So the grain A growth until the grain boundary C reached the dashed line and the grain boundary will stop. This dashed line is the limit of the grain boundary migration of grain boundary C. But if the triple junctions which are indicated as red dots move along grain boundary D and F, the curvature of grain boundary C is maintained and the grain boundary migration will occur continuously.

Considering such a geometrical condition, for a certain grain to grow abnormally, it is necessary that the triple-junction line at the growth front should have a high migration rate. Then when the triple junctions can move along grain boundary D and F? It can occur when the solid-state wetting occurs. If the grain boundary energies shown in figure 1.1 satisfy below two equations, the solid-state wetting occurs and the grain boundary migration occurs continuously.

$$\gamma_{\mathrm{D}} > \gamma_{\mathrm{E}} + \gamma_C \tag{1.1}$$

$$\gamma_{\mathrm{F}} > \gamma_G + \gamma_C \tag{1.2}$$

This condition is the wetting condition. If the energies of the grain boundaries connected to the triple junction satisfy the wetting condition, the triple junction wetting occurs and the triple junction move fast along the grain boundary which has high energy.

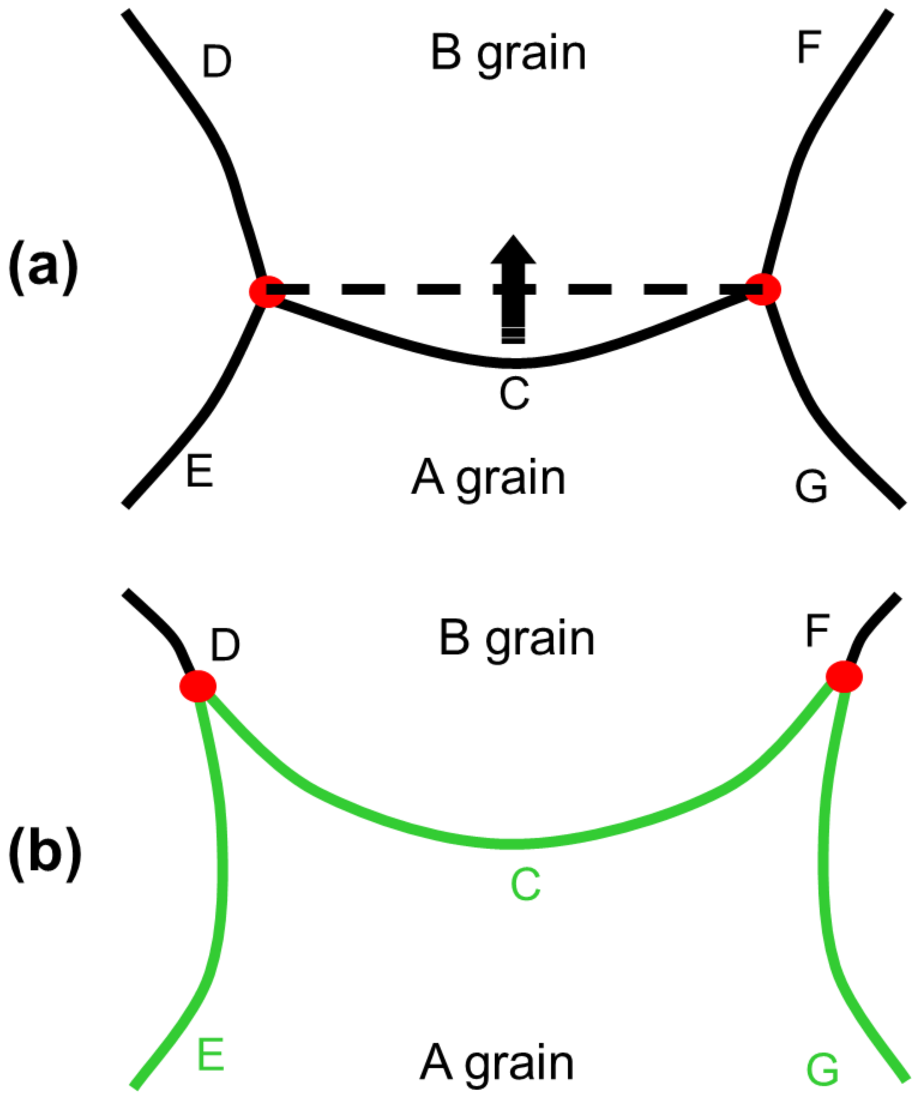

Figure 1.1 Schematics of grain boundary migration when the triple junctions are (a) fixed and (b) moved, which shows the relation between grain boundary migration and triple junction

1.3 Sub-boundary enhanced solid-state wetting

In order to understand the mechanism of AGG, it is critical to find out the condition under which the triple-junction line should migrate at a high rate. Figure 1.2 is the schematics about increase of wetting probability by sub-boundary. In figure 1.2 (a), to occurs wetting, the grain boundary energies satisfy this condition

$$\gamma_{\mathrm{AB}} > \gamma_{\mathrm{AC}} + \gamma_{BC}$$

Normally, the grain boundary energy is not so different to enhance solid-state wetting like the figure 1.2 (a). But if the grain B has extremely similar orientation to grain A; if the grain boundary AB is sub-boundary, wetting condition is easily satisfied and wetting occurs. For example, even though grain C is changed to grain D, if the grain D has the even small difference between the grain boundary energies, the wetting can occur.

Hwang et al. [16-19] showed by Monte Carlo (MC) and phase field model simulations that the migration rate of the triple-junction line increases abruptly when solid-state wetting occurs. To explain the selective AGG of Goss grains in Fe-3%Si, Hwang et al. [17, 20-22] suggested based on MC and phase field model simulations that if Goss grains have sub-boundaries of very low energy, the wetting probability increases so high that Goss grains can undergo exclusive AGG. Based on these results, Hwang et al. [20, 23, 24] proposed sub-boundary enhanced solid-state wetting as a mechanism of AGG. According to this mechanism, sub-boundaries with very low misorientation angles should exist exclusively in abnormally-growing grains, which was experimentally confirmed by Park et al. [22], Ushigami et al. [25], Dorner et al. [26] and Shim et al. [27] in Fe-3%Si steel and by Park et al. [28] in Al 5052 alloy.

Park et al. studied about the reason why the Goss grains have sub-boundaries exclusively based on the deformation behavior during cold rolling using numerical analysis, the finite element method (FEM) [29]. According this study, the Goss grain survives after 87% cold reduction despite the instability of the Goss orientation under plane strain deformation and the stored energy in Goss grain is lower than other grains formed after cold rolling. Thus, during primary recrystallization, the remaining Goss grain undergoes only recovery and the sub-boundary can be formed only in the Goss grain exclusively.

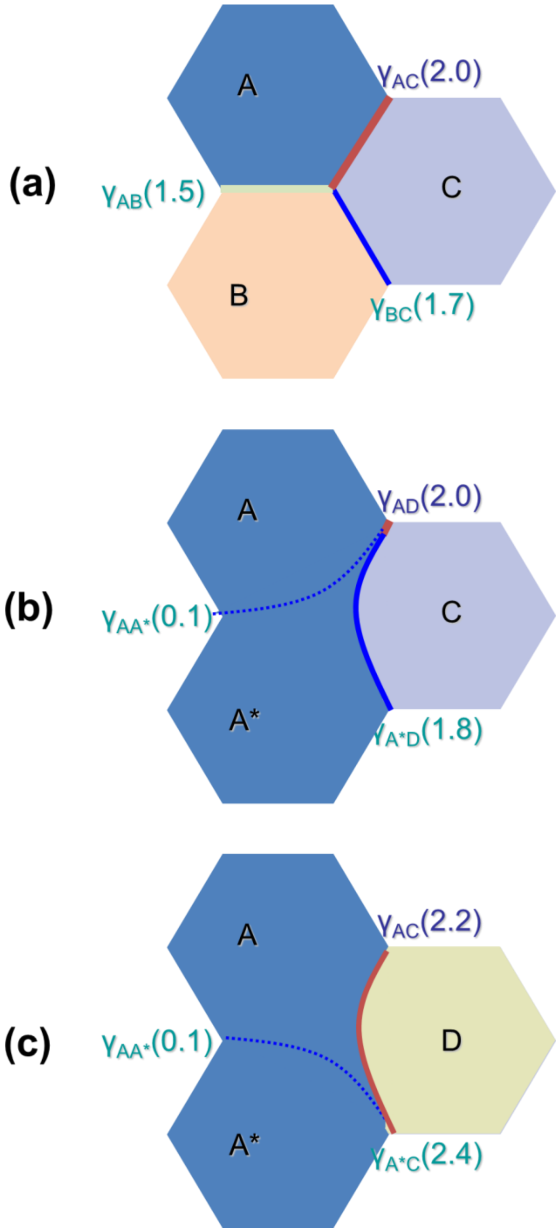

Figure 1.2 Schematics about increase of wetting probability by sub-boundary; the case (a) without sub-boundary and (b, c) with sub-boundary

CHAPTER 2

Misorientation angle analysis near the growth front of abnormally growing grains in 5052 aluminum alloy

2.1 Mechanism of sub-boundary enhanced solid-state wetting

To examine a wetting morphology evolved when wetting along a triple junction line occurs, we use the three-dimensional MC simulation based on the algorithm reported by Srolovitz et al. [30]. For the simulation, 160 × 160 × 160 sites of a three-dimensional simple cubic lattice are used. In order to focus on the wetting morphology, 4 grains in contact are considered in the simulation using a fixed boundary condition. The condition for a grain A to wet along the triple junction line made by three grains B, C and D is expressed as [31].

$$\gamma_{BC} + \gamma_{\mathrm{CD}} + \gamma_{\mathrm{BD}} > \sqrt{3}(\gamma_{\mathrm{AB}} + \gamma_{\mathrm{AC}} + \gamma_{\mathrm{AD}}), \tag{2.1}$$

where γ is the grain boundary energy and the subscript represents the grain boundary. For example, the subscript BC represents the grain boundary between grains B and C. When the grain boundary energies between grain A and grains B, C or D were given as 1 and those between grains B and C, grains C and D and grains B and D were given as $\sqrt{3}$, the grain A undergoes the triple junction wetting and its morphology evolved by the three-dimensional MC simulation is shown in Fig.

2.1.

Fig. 2.1a and 2.1c show how the microstructure of triple junction wetting is observed two-dimensionally on a polished surface of real samples when observed on a two-dimensional section parallel to the triple junction line of grains B, C and D. Likewise, Fig. 2.1b and 2.1d show the microstructure observed on the polished surface when observed on a two-dimensional section vertical to the triple junction line. The penetrating morphology in Fig. 2.1a and 1c indicates that the triple junction migrates abruptly ahead of the grain boundary. This means that solid-state wetting increases the migration rate of the triple junction in an abrupt manner. Note that in Fig. 2.1, the grain boundaries of the penetrating grain A have characteristics of a negative or inward curvature. This negative curvature indicates that the grain A is growing instead of shrinking. Especially the grain A in Fig. 2.1b and 2.1d have three sides on the two-dimensional section. It is highly in contrast with the case of isotropic grain boundary energy where the grain with sides less than 6 in a two dimension has a positive curvature and shrinks. Therefore, a penetrating morphology as shown in Fig. 2.1a and 1c and a three-sided grain with negative curvatures as shown in Fig. 2.1b and 2.1d can be a microstructural evidence for solid-state wetting. In Fig. 2.1b and 2.1d, the sum of the inner angles of the three-sided grain A should be less than 180° to satisfy the wetting condition. This condition, which is equivalent to Eq. (1), is known as the criterion of the triple junction wetting [21].

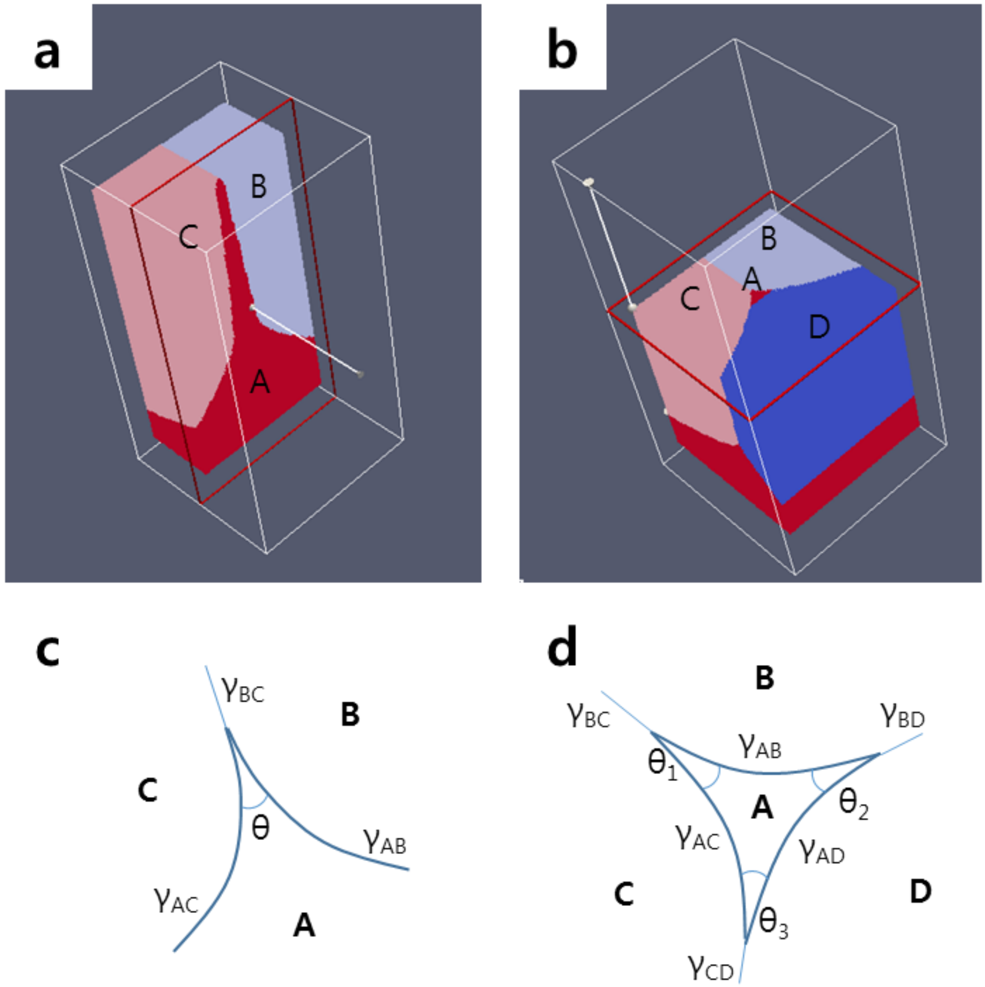

Figure 2.1 Two-dimensional microstructure of three-dimensional triple junction wetting morphology made by MC simulation (a), (c) Parallel section to the wetting direction (b), (d) Vertical section to the wetting direction.

If the grains A and D share a sub-boundary of extremely low angle. Then, the energy of the grain boundary between grains A and D would be negligibly low compared to those of the other 5 grain boundaries in Eq. (1). Therefore, the misorientation angle between grains A and D as well as γ_{AD} can be approximated as zero. This approximation is supported by the previous report that the sub-boundaries observed in the abnormally-growing Goss grains have misorientation angles of ~ 0.15° and ~ 0.17° with their energy roughly 20 times less than that of high angle boundaries [10]. If the misorientation angle between grains A and D is approximated as zero, it can be further approximated that

$$\gamma_{AB} \approx \gamma_{BD} , \quad \gamma_{AC} \approx \gamma_{CD} \tag{2.2}$$

Then, the wetting condition of Eq. (2.1) is simplified as [31].

$$\gamma_{BC} > (\sqrt{3}-1)(\gamma_{AB} + \gamma_{AC}) \tag{2.3}$$

On the other hand, the misorientation angles between grains A and B, grains A and C and grains B and C can be determined experimentally using EBSD from the microstructure of the penetrating morphology on a two dimensional section of real samples as shown in Fig. 2.1a and 2.1c. It should be noted that the sub-boundary angle between grains A and D is not resolved by EBSD. Eq. (2.3) indicates that if γ_{BC} is 0.732 times higher than the sum of γ_{AB} and γ_{AC}, the triple junction wetting would occur. Therefore, the penetrated grain boundary is expected to have high energy. In agreement with this analysis, all penetrated grain boundaries, which were observed at the growth front of abnormally growing grains in Fe-3%Si steel [32] and Al 5052 alloy[31], had high misorientation angles.

If the measured misorientations are converted to grain boundary energies using such as Read-Shockley equations [21, 24, 33], it can be checked whether the wetting microstructure such as shown in Fig. 2.1a and 2.1c should satisfy the wetting condition of Eq. (2.3) or not. In this paper, we examined if the wetting condition of Eq. (2.3) is satisfied by estimating grain boundary energies from misorientation measurements of the three grains in the penetrating morphology. Some matrix grains away from the growth front of abnormally growing grains turned out to have the same crystallographic orientation as that of the abnormally growing grain. Considering the wetting mechanism, these matrix grains are expected to have formed by wetting along the triple junction line at the growth front of an abnormally growing grain. Since these grains would correspond to the microstructure of Fig. 2.1b and 2.1d, they look isolated when observed on a two-dimensional section vertically to the triple junction line. If they are observed on each serial section, it would reveal that they are identical to the abnormally growing grain. Based on these analyses, it was suggested that AGG in aluminum 5052 alloy also occurs by sub-boundary enhanced solid-state wetting mechanism.

2.2 Experimental Procedure

Commercial aluminum alloy AA 5052 (Al-2.5%Mg-0.3%Cr-0.3%Fe-0.2%Si) was used to study the morphology of abnormally growing grains. The hot rolled AA 5052 sheet with 10 mm thickness was cold-rolled to 2 mm. In order to induce the primary recrystallization, the cold rolled sheet was annealed in the box furnace at 400 ˚C for 60 min. After primary recrystallization, AA 5052 sheet was further annealed at 500 ˚C for 30 min to obtain the initial stage of AGG. Then the sample was polished and macro etched with 35% HCl solution to identify abnormally growing grains and their locations were marked by the indenter in order to easily trace out for EBSD measurements.

The penetrating morphology such as shown in Fig. 2.1a and 2.1c was searched at the growth front of abnormally growing grains. After the misorientation angles were measured in the penetrating morphology by EBSD, they were converted to the grain boundary energy by modified Read-Shockley functions expressed as [21, 24, 33]

$$E(S_i,S_j) = \begin{cases} E_0 \frac{\theta}{\theta_{RS}}\left[1 - \ln\left(\frac{\theta}{\theta_{RS}}\right)\right], & \theta < \theta_{RS} \quad \text{(low angle boundary)} \\ r', & \theta \geq \theta_{RS} \quad \text{(high angle boundary)} \\ E_{CSL} + (\overline{r'} - E_{CSL}) \frac{w}{v_m}\left[1 - \ln\left(\frac{w}{v_m}\right)\right], & \frac{w}{v_m} < 1 \quad \text{(CSL boundary)} \end{cases} \quad (2.4)$$

where S_i and S_j are the orientations of adjacent grains and $E(S_i,S_j)$ is the grain boundary energy. θ is the misorientation angle and θ_{RS} is the maximum misorientation angle of low angle boundary, 15°. r' is the energy of high angle boundaries. w is the deviation angle between the real misorientation and the misorientation of the exact CSL boundary and v_m is the maximum deviation angle, $\theta_{RS}/\Sigma^{\frac{1}{2}}$ [34, 35]. E_{CSL} is the grain boundary energy of the exact CSL boundary. E_0, E_{CSL} and r' are set by the result of the mesoscale simulation performed by Kim et al. [35, 36].

In order to examine how the morphology of abnormally growing grains changes along the sample thickness, the sample was serially polished, observed and measured by EBSD on each section. Since the average matrix grain size was 50 μm, the thickness removed by polishing was made 10 μm at each step. The sample height of each step was measured by a thickness gauge (Mitutoyo). The misorientations on each section were measured by EBSD. The step size of EBSD, which was attached to a field-emission scanning electron microscope (JSM-6500F, JEOL), was 3 μm. The EBSD data were analyzed using the software TSL/EDAX. The grain-boundary misorientation angle and the CSL relation were calculated up to ∑21 using Brandon's criteria[34].

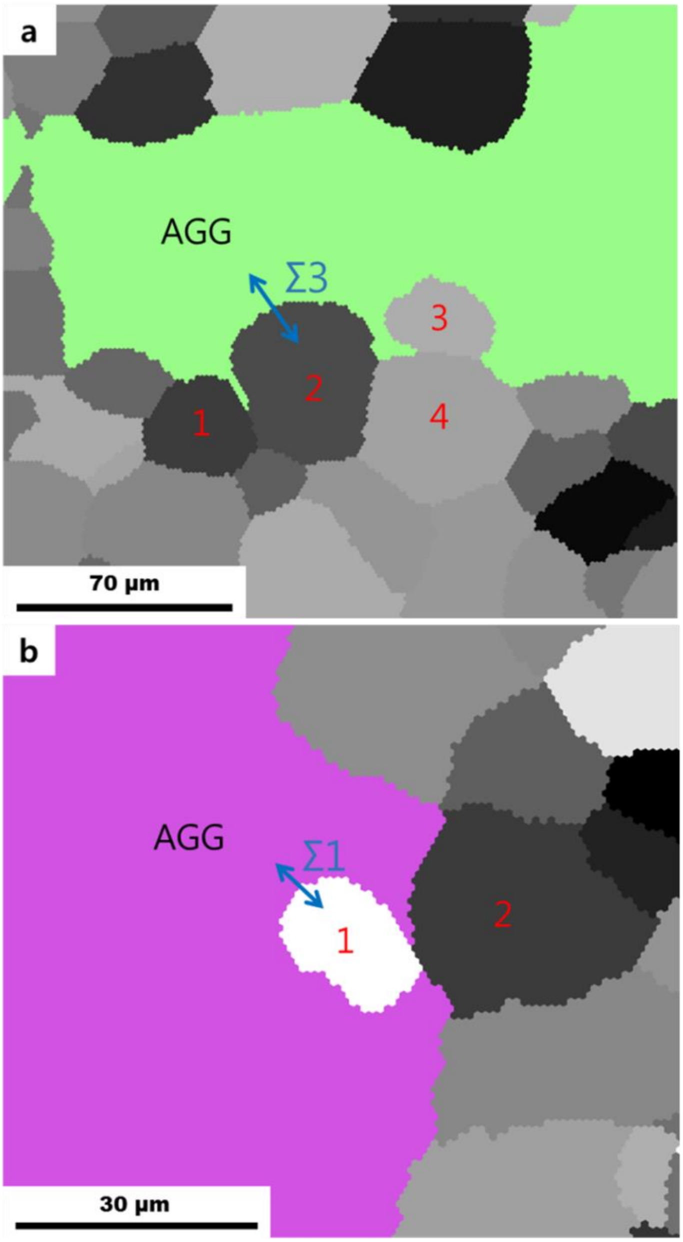

Figure 2.2 EBSD images with wetting morphologies near the growth fronts of abnormally growing grains in aluminum alloy 5052: (a) orientation of (1 -8 13)[7 22 13] and (b) orientation of (-10 11 24)[7 2 2].

2.3 Misorientation angle analysis near the growth front of abnormally growing grains in 5052 aluminum alloy

Fig. 2.2 shows the microstructures obtained by EBSD near the growth front of abnormally growing grains. Two abnormally-growing grains in Fig. 2.2a and 2.2b, where were evolved after annealing for 20 min at 500℃, are designated as ‘AGG’, being colored in green and purple respectively. To distinguish clearly between abnormally and normally growing grains, the normal grains are represented by the average image quality obtained by EBSD. Orientations of the abnormally growing grains and neighboring matrix grains numbered in Fig. 2.2 are listed in Table I. Misorientations measured by EBSD and grain boundary energies between AGG grain and numbered grains and between two numbered grains in Fig. 2.2a and 2.2b, which were estimated from misoreintations and Eq. (2.4), are listed in Table II.

Fig. 2.2a shows that the grain boundaries between grains 1 and 2 and between grains 2 and 3 are penetrated by the abnormally-growing grain. Similarly, Fig. 2.2b shows that the grain boundaries between grains 1 and 2 are shown to be penetrated. As mentioned in the Background section, these penetration microstructures would be the two-dimensional section of the three-dimensional wetting microstructure sectioned parallel to the triple junction line as shown in Fig. 2.1a and 2.1c.

To satisfy the wetting condition of Eq. (2.3), the penetrated grain boundary should have relatively high energy and the grain boundaries shared by the penetrating grain, which grows abnormally, should have relatively low energy. In Fig. 2.2a, the misorientation angles for the penetrated grain boundaries between grains 1 and 2 and between grains 2 and 4 are respectively 46.6˚/[9 5 24] and 58.3˚/[13 10 15], both of which are high energy boundaries. However, the misorientation angle for the penetrating grain boundary between the abnormally growing grain and the grain 2 is 58.4˚/[17 16 17], which has ∑3 relationship according to Brandon's criteria. Likewise, the misorientation angle for the penetrated grain boundary between grains 1 and 2 in Fig. 2b is 46.0˚/[7 1 18], which is a high energy boundary. But the grain boundary between the abnormally growing grain and the grain 1 has the low misorientation angle, 3.0˚/[15 4 20], which is a ∑1 boundary of low energy. Therefore, these misorientation angles are in favor of satisfying the wetting condition of Eq. (2.3).

Figure	Grain number	Orientation
2a	1	(1 1 10)[15 -5 -1]
	2	(-2 0 5)[-10 21 -4]
	3	(7 18 20)[-2 23 -20]
	4	(17 19 23)[9 -2 -5]
	AGG	(1 -8 13)[7 22 13]
2b	1	(-10 13 25)[19 5 5]
	2	(-1 -5 18)[13 1 1]
	AGG	(-10 11 24)[7 2 2]

Table 2.1 Crystallographic orientations of grains in Fig. 2

It can be checked whether the grain boundary energies estimated from misorientations of these penetrating microstructures should satisfy the wetting condition of Eq. (2.3). Table II shows that the grain boundary between grains 2 and AGG in Fig. 2a has very low grain boundary energy, 0.42 J/m^2, because the grain 2 has ∑3 relationship with the abnormally growing grain. Table II also shows that the grain boundary energies between grains 1 and 2 and between grains 1 and AGG in Fig. 2.2a are respectively 1.49 J/m^2 and 1.36 J/m^2. Since 0.42 J/m^2 + 1.36 J/m^2 = 1.78 J/m^2, showing that the summation of the penetrating grain boundary energies is equal to 1.78 J/m^2, and the penetrated grain boundary energy is 1.49 J/m^2, the grains 1, 2 and AGG in Fig. 2.2a satisfy the wetting condition of Eq. (2.3). Likewise, since 0.42 J/m^2 + 1.24 J/m^2 = 1.66 J/m^2 in Table II, showing that the summation of the penetrating grain boundary energies between grains 2 and AGG and between grains 3 and AGG is equal to 1.66 J/m^2, and the penetrated grain boundary energy is 1.68 J/m^2, the grains 2, 3 and AGG in Fig. 2.2a satisfy the wetting condition of Eq. (2.3). Similarly, in Table II and Fig. 2.2b, 0.45 J/m^2 + 1.47 J/m^2 = 1.92 J/m^2, showing that the summation of the penetrating grain boundary energies between grains 1 and AGG and between grains 2 and AGG is equal to 1.92 J/m^2, and the penetrated grain boundary energy is 1.49 J/m^2, the grains 1, 2 and AGG in Fig. 2.2b satisfy the wetting condition of Eq. (2.3).

The same analyses on 10 additional penetrating microstructures satisfy the energetic condition of wetting along the triple junction line. Much more data may be needed to make a statistically meaningful conclusion. In relation to this aspect, however, Park et al.[32] examined 34 penetrating microstructures at the growth front of abnormally growing Goss grains in Fe-3%Si steel and found out that one of the penetrated boundaries have low misorientation angles less than 20^{o}. Besides, Park et al.[31] examined 84 penetrating microstructures at growth front of abnormally growing grains in Al 5052 alloy and found out that none of the penetrated grain boundaries have low misorientation angles less than 15^{o}. Considering these, it is highly probable that the penetrating morphologies at the growth front of abnormally growing grains in Fig. 2.2a and 2.2b have formed by wetting along the triple junction line.

Wetting along the triple junction line ends at the four grain corner, which is connected with other three triple junction lines. If any of three triple junctions satisfies the wetting condition of Eq. (2.3), wetting would continue. Therefore, if the wetting probability is higher than 1/3, wetting would continue, resulting in AGG as shown using MC simulations by Ko et al. [21]. When an abnormally growing grain undergoes solid-state wetting along triple junctions, the growth front would proceed not uniformly but highly non-uniformly because some triple junctions can satisfy Eq. (2.3) while other ones cannot. Because of this, the growth front can be very irregular and some growth front can be observed to be away from the abnormally growing grain on the two-dimensional section. Such a growth front may be regarded as one of matrix grains if their orientation is not determined by

EBSD. When such a growth front is measured by EBSD, it would have the same orientation as that of the abnormally growing grain.

Fig.	Grains		Misorientation axis	Misorientation angle(°)	CSL type	Grain boundary energy (J/m^2)
2a	1	2	[9 5 24]	46.6	-	1.49
	1	AGG	[4 17 2]	37.7	-	1.36
	2	3	[13 10 15]	58.3	-	1.68
	2	4	[4 5 7]	40.9	-	1.41
	2	AGG	[17 16 17]	58.4	Σ3	0.42
	3	4	[3 7 1]	45.4	-	1.49
	3	AGG	[12 13 3]	29.9	-	1.24
	4	AGG	[2 2 3]	43.4	-	1.45
2b	1	2	[7 1 18]	46.0	-	1.49
	1	AGG	[15 4 20]	3.0	Σ1 (low angle)	0.45
	2	AGG	[9 2 3]	44.6	-	1.47

Table 2.2 Misorientations and grain boundary energies in Fig. 2

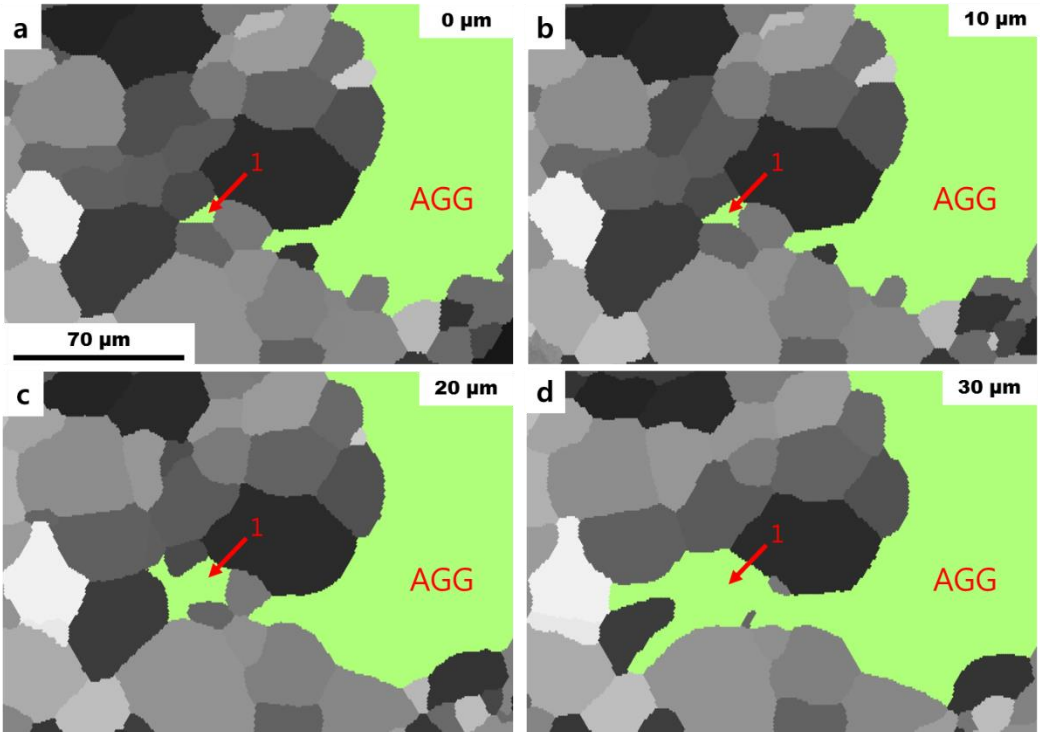

Figure 2.3 Serially sectioned EBSD microstructures of four-sided grain with negative boundary curvature near an abnormally growing grain showing that this grain is connected with the abnormally growing grain: depth of (a) 0 μm (b) 10 μm (c) 20 μm and (d) 30 μm from surface.

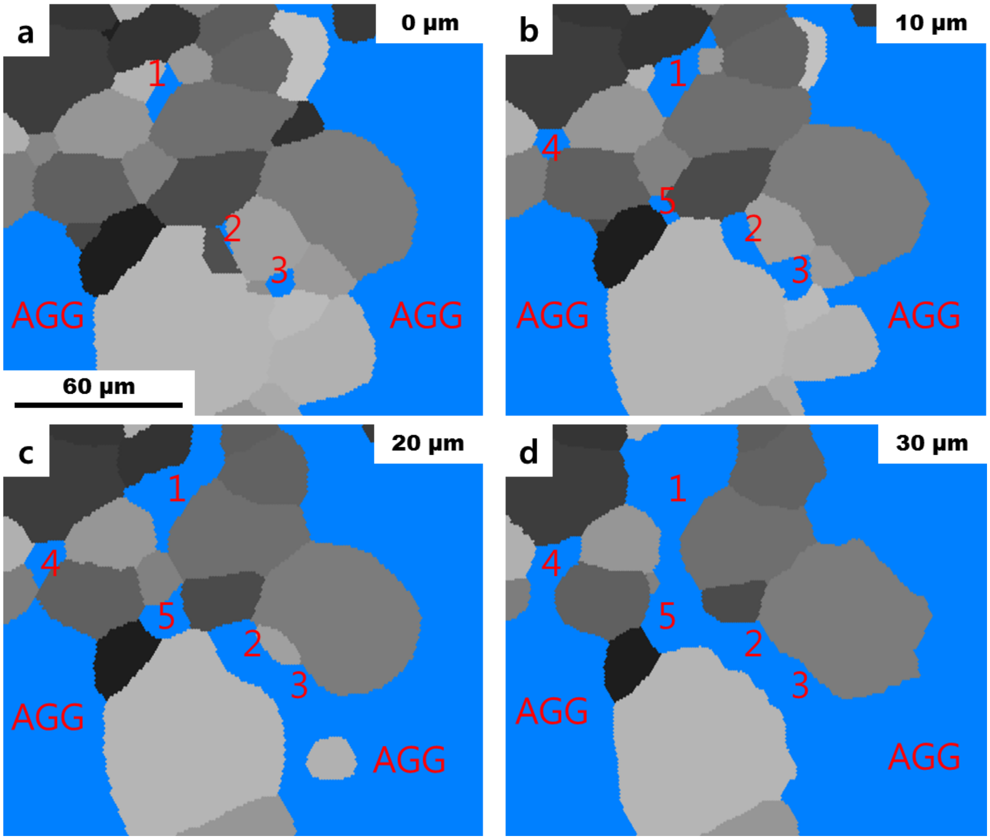

Figure 2.4 Serially sectioned EBSD microstructures of grains with crystallographic orientation of the abnormally growing grain showing that these grains are connected with the abnormally growing grain: depth of (a) 0 μm (b) 10 μm (c) 20 μm and (d) 30 μm from surface.

Such a case is shown in Fig. 2.3a and 2.4a. The grain 1 in Fig. 2.3a look separate from the AGG grain colored in green. However, the grain 1 has the same orientation as the AGG grain, indicating the possibility that the grain 1 is the growth front of the AGG grain. This possibility can be checked by the serial section of the sample and by the EBSD measurements on each section. Fig. 2.3a - 2.3d show the serially-sectioned EBSD images of the same region by preparing each section after the removal of 10 μm by polishing. Fig. 2.3 is the grain average direction grayscale map scaled according to the crystallographic normal direction using the TSL/OIM software.

The grain 1 in Fig. 2.3b, which is larger than the grain 1 in Fig. 2.3a, is four-sided with a negative grain boundary curvature, indicating that this grain is growing instead of shrinking. The grain 1 in Fig. 2.3c is even larger than the grain 1 in Fig. 2.3b. Finally, the grain 1 in Fig. 2.3d is shown connected with the AGG grain. This means that the grain 1 in Fig. 2.3, which is identical to the AGG grain, being connected three-dimensionally, is the growth front undergoing wetting along the triple junction line. The wetting direction of the grain 1 in Fig. 2.3a and 2.3b is vertical to the two-dimensional section of the microstructure.

Fig. 2.4 shows the grain average direction grayscale maps near the growth front of another abnormally growing grain colored in blue. Like Fig. 2.3, each map in Fig. 2.4a-2.4d shows a serially sectioned microstructure with a section thickness of 10 μm. The grains 1, 2 and 3 in Fig. 2.4a look separate from the AGG grain colored in blue. Especially, the grains 1 and 2 in Fig. 2.4a are respectively four-sided and three-sided with negative grain boundary curvatures. All grains in blue have the same crystallographic orientation as that of the AGG grain.

The size of grains 1, 2, and 3 in Fig. 2.4a becomes larger as the polishing goes on as revealed by Fig. 2.4b, 2.4c and 2.4d. The grains 2 and 3 become connected each other in Fig. 2.4b. The grains 4 and 5 newly appear in Fig. 2.4b. In Fig. 2.4c, the grains 2 and 3 are connected with the AGG grain. Finally, in Fig. 2.4d, all the blue grains are connected with the AGG grain. The serial-section images of Fig. 2.4a-2.4d indicate that the three-dimensional morphology of the blue abnormally growing grain has a very irregular shape and the triple junction wetting occurred in the direction from Fig. 2.4b to Fig. 2.4a or from the interior to surface of the sample.

Results and analyses of Fig. 2.2, 2.3 and 2.4 indicate that wetting along the triple junction line occurs actively at the growth front of the abnormally growing grains in AA 5052 alloy. They also indicate that wetting at the growth front occurs very irregularly, producing a highly irregular three-dimensional morphology. As a result, the growth front appears to be separate from the abnormally-growing grain on a two-dimensional section. Such highly irregular growth would be responsible for the high frequency of peninsular-shaped grains at the growth front and island-shaped grains inside the abnormally growing grain, which is a well-known growth feature of AGG [37-39].

CHAPTER 3

Reproduction of three-dimensional morphology of abnormally growing grains by MC simulation

3.1 Introduction

Using EBSD, synchrotron or XRD, the observation of the three-dimensional morphologies of real Goss grains without destruction is extremely difficult. Using EBSD with FIB, the researches about three-dimensional morphology of materials are progressed [40, 41] but the rage of observation is too small to observe the abnormally growing grains. Synchrotron is also used to research three-dimensional morphology of ceramic or metal-organic materials [42, 43] but the penetration depth for metals including Fe-3%Si steel is too small to observe the abnormally growing Goss grain.

Because of this difficulty for observing the three-dimensional morphology of abnormally growing grains, there are many efforts to reproduce the morphology of abnormal grain growth with simulation [30, 44-47]. Only the MC simulation which is performed with precipitates, sub-boundaries and the real orientation demonstrates properly the two-dimensional observed microstructure of real Goss grains [24]. Because the two-dimensional microstructure of simulated Goss grain is extremely similar to that of real Goss grain, the three-dimensional morphology of real Goss grain can be predicted from that of simulated Goss grain. So the three-dimensional morphology of simulated Goss grain should be analyzed.

3.2 Reconstruction of the three-dimensional morphology of abnormally growing grain

To compare the three-dimensional morphology of the abnormally growing grain and the normally growing grain, simulation is done with and without precipitates and sub-boundaries. Without precipitates and sub-boundaries, as the prediction, the normal grain growth occurs. To obtain the tree-dimensional morphology of Goss grain, simulation data was converted to three-dimensional image by MATLAB.

Figure 3.1(a) and (b) are the three-dimensional morphologies of a normally growing grain and an abnormally growing grain. The simulation for normal grain growth is done for 750 MCSs, during the simulation for abnormal grain growth is done for 10000 MCSs. The growth rate in the initial stage is faster when the grain grows normally then abnormally. The normally growing grain has facet grain boundaries and the morphology of the grain is simple. On the other hand, the abnormally growing grain has extremely irregular shape.

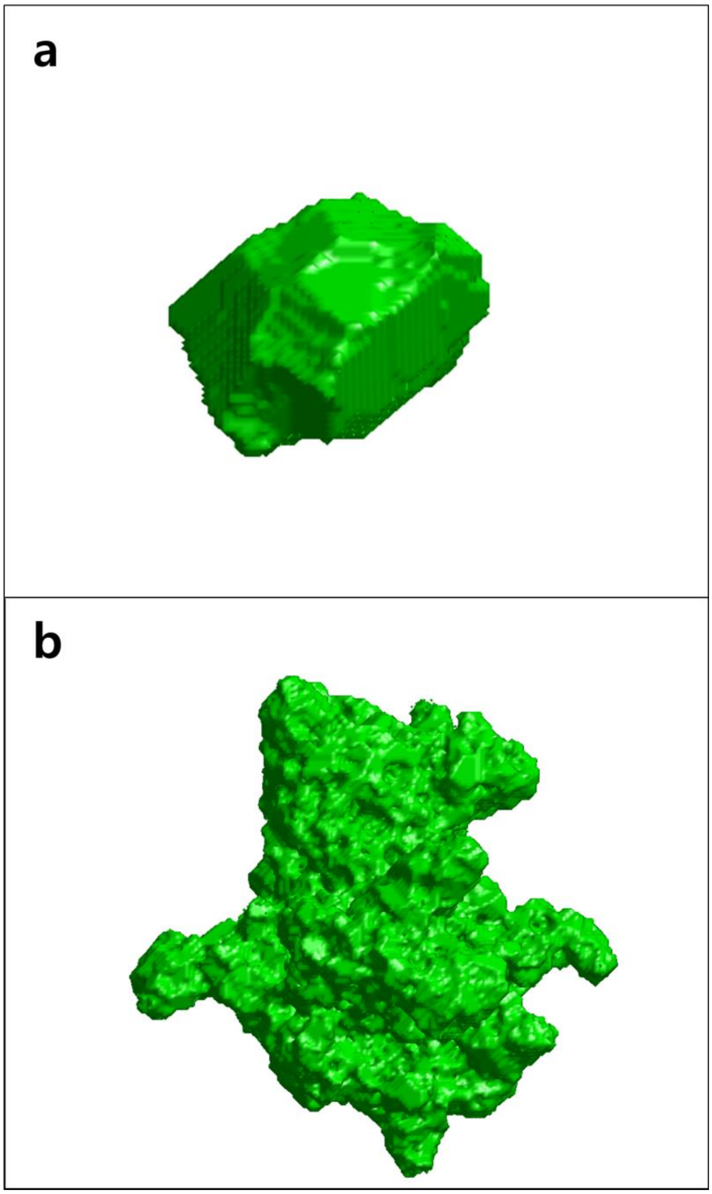

Figure 3.1 The three-dimensional morphology of (a) the normally growing grain and (b) the abnormally growing grain

3.3 The time evolution of the abnormally growing grain morphology reconstructed from the simulation data

There are few ways to observe time evolution of the three-dimensional morphology. Using white synchrotron radiation is the one example of these ways [48]. But because of the penetrating depth for metals, it is impossible to observe the whole three-dimensional morphologies of abnormally growing grains.

The advantage of the simulation is that the inside of sample can be observed easily. Figure 3.2 is the three-dimensional morphology time evolution of the simulated Goss grain after 0, 1250, 2500, 3750, 5000, 6250, 7500, 8750 and 10000 MCSs. In figure 3.2, the green grain at the center is an abnormally growing grain and other matrix grains are not presented to observe whole three-dimensional morphology of the abnormally growing grain. The grain growth does not occur equally at the grain boundary of Goss grain. Because of this, the abnormally growing grain has extremely irregular shape. The parts indicated by dashed circle seems like the wetting occurs.

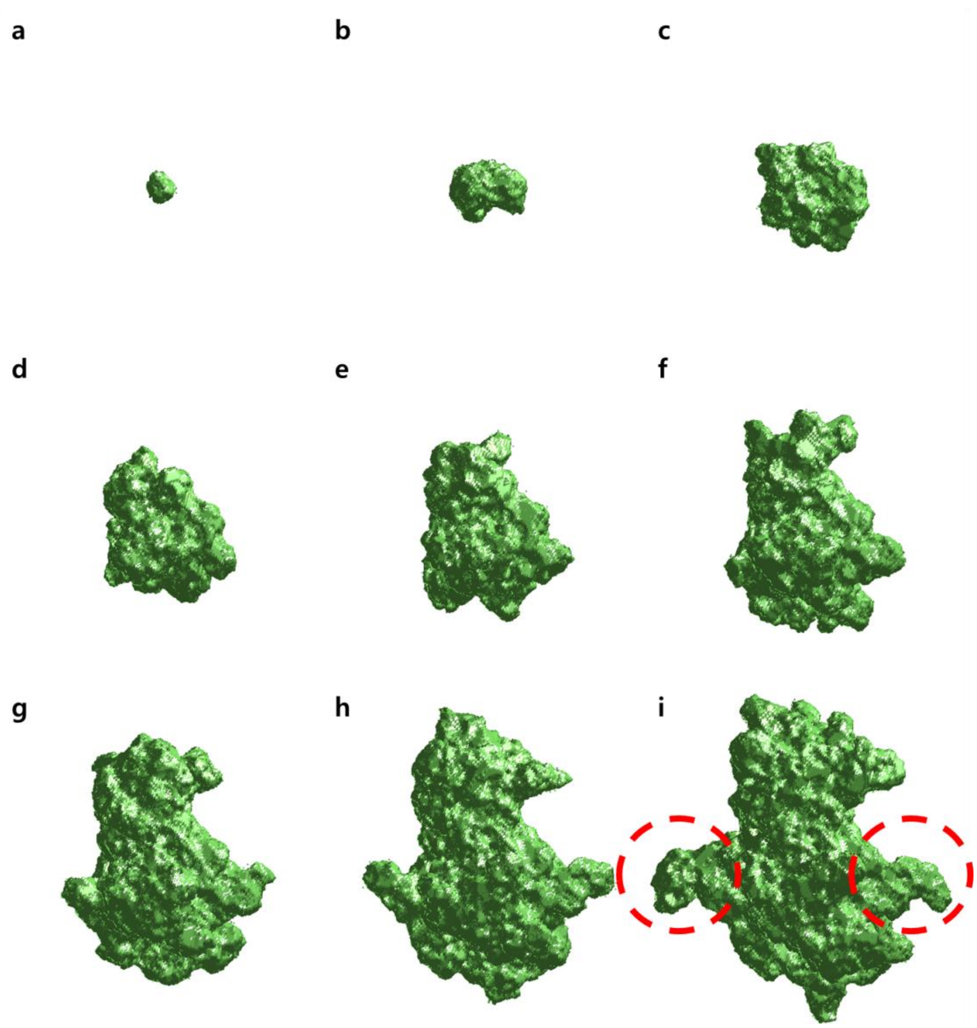

Figure 3.2 The three-dimensional morphologies of the simulated Goss grain after (a) 0 MCS, (b) 1250 MCSs, (c) 2500 MCSs, (d) 3750 MCSs, (e) 5000 MCSs, (f) 6250 MCSs, (g) 7500 MCSs, (h) 8750 MCSs and (i) 10000 MCSs

3.4 The relation between two-dimensional microstructure and three-dimensional morphology

Inokuti et al. [49] observed that the Goss grains exist near each at the initial stage of secondary recrystallization and these grains get together as the secondary recrystallization goes on. Ko et al [50] observed these grains are connected three-dimensionally to each other by serial sectioning.

3.4.1 Serial sectioning and three-dimensional morphology

Figure 3.3 is the two-dimensional sectioned images of a Goss grain and the sectioning location. In figure 3.3 (a), there are 3 grains separated. But figure 3.3 (j) shows that the grains are connected three-dimensionally to each other. When z value becomes lower, the 3 grains become the one grain in figure 3.3 (c). When the z value is 105, the new grain appears indicated by dashed red circle in figure 3.3 (e). And this grain is also connected to the other grain in figure 3.3 (m). And this grain becomes a part of the main grain in figure 3.3 (f). When the z value is 85, another separated grain indicated by dashed blue circle appears in figure 3.3 (g) and it is also connected to the other grain in figure 3.3 (o). This grain becomes a part of the main grain in figure 3.3 (h).

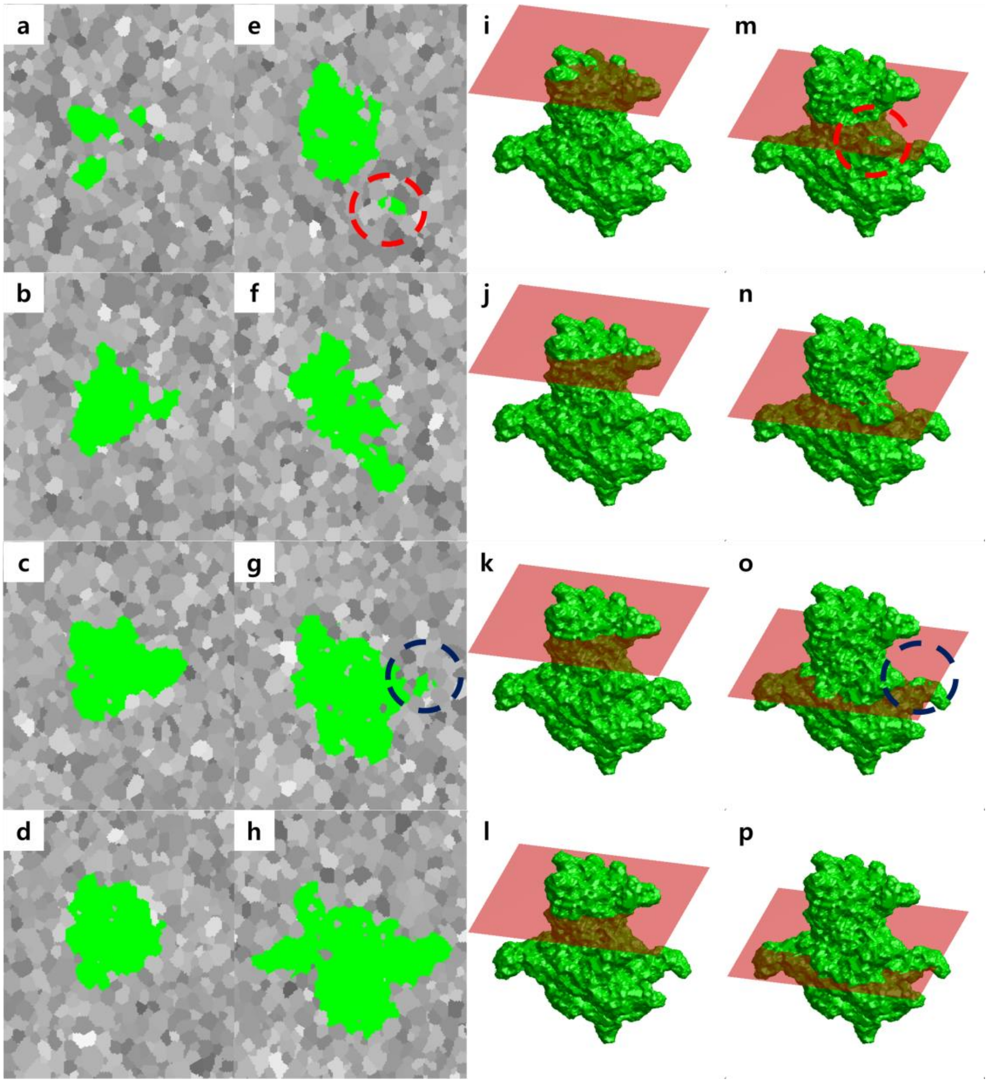

Figure 3.3 The sectioned images and the sectioned plane of the abnormally growing grain at (a, i) z=145 (b, j) z=135 (c, k) z=125 (d, l) z=115 (e, m) z=105 (f, n) z=95 (g, o) z=85 and (h, p) z=75

3.4.2 Time evolution of the two-dimensional microstructure and three-dimensional morphology

Figure 3.4 is the time evolution of sectioned Goss grain images and the sectioned plane. Figure 3.4 shows that the other matrix grains are not changed during the abnormal grain growth occurs. The growth front indicated by solid blue line does not changed until 9750 MCSs. But the two-dimensionally separated grains indicated by dashed red line appear in figure 3.4 (c) and connected to the other grain in figure 3.4 (d) removing the growth front which is indicated by solid blue line. These unique behaviors of growth front during secondary recrystallization are already reported [51] and the simulation reproduce these behaviors. As a result, it can be predicted that the grain growth occurs by sub-boundary enhanced solid-state wetting mechanism.

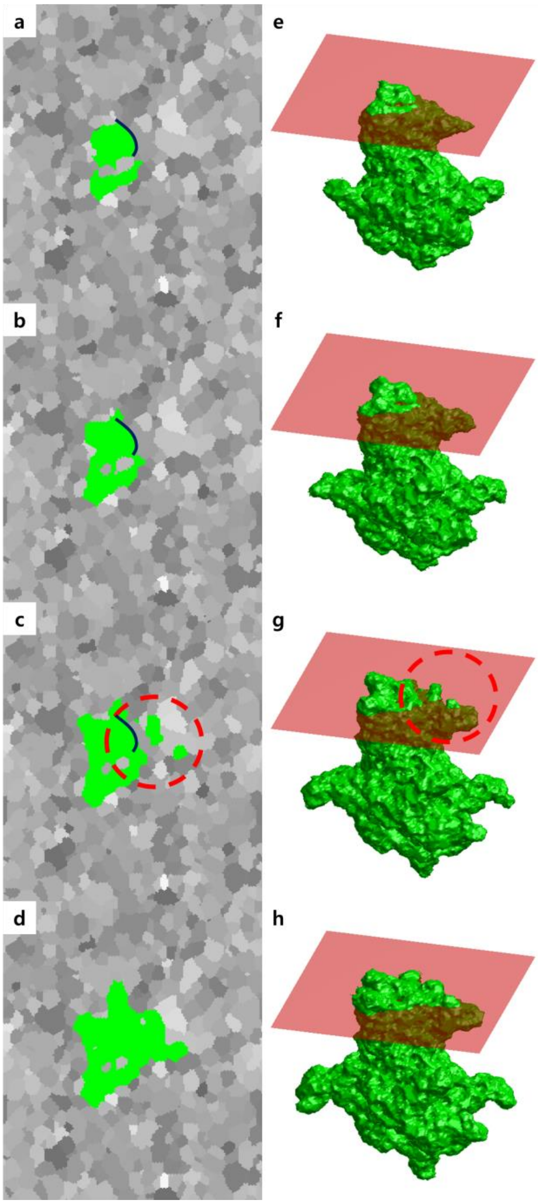

Figure 3.4 The sectioned imaged and the sectioned plane of the abnormally growing grain after (a, e) 8750 MCSs (b, f) 9250 MCSs (c, g) 9750 MCSs (d, h) and 10250 MCSs

CHAPTER 4

Observation of three-dimensional morphology of abnormally growing grains by serial section

4.1 Experimental procedure

To observe the three-dimensional morphology of abnormally growing grains, an ingot of Fe-3%Si steel, which is the material for grain-oriented electrical steel, was used. AlN is employed as an inhibitor of grain growth to enhance abnormal grain growth. The steel ingot was hot rolled to 2.3mm and was cold rolled to 0.3mm by the thickness reduction of 87%. At the temperature of 850℃ for 150s in a wet 10% H_2-N_2 atmosphere, the specimens were primary recrystallized and decarburized. To obtain the initial stage of abnormal grain growth, the primary recrystallized specimens were heated in a stepwise fashion at 5℃/min in a H_2 atmosphere up to 1050℃, held for 5 min and air cooled to room temperature. The initial stage of abnormal grain growth was identified by macro etching. The secondary recrystallized specimens were macro etched by 36% HCl soluation at 100℃ for 10~20s and cleaned by alcohol. Abnormally growing grains in the specimens with the size less than 1mm were selected. The specimen around the abnormally growing grains were cut into the size of 5mm x 5mm and mounted with polycarbonate resin to section serially.

For serial sectioning, Robo-Met.3D made by UES was used. The machine automatically performed a series of steps for serial sectioning and obtaining two-dimensional optical microscopic images of each section. The series of steps consist of polishing, cleaning, etching, rinsing the etching solution, drying and observing with optical microscopy. At the step of polishing, the specimens were polished by 1 μm diamond suspension with the force of 15N for 1 min. After polishing, suspension was cleaned by alcohol and the sample was etched by 5% HNO_3 solution for 30s. The etched sample was washed by alcohol and observed by the optical microscopy. The two-dimensional optical microscopic images were converted to the three-dimensional reconstructed image by Avizo Fire 7.

4.2 Three-dimensional morphology reconstructed by serial sectioned images of Goss grain

Figure 4.1 is the optical microscopic images of abnormally growing grains A, B and C in etched specimens. Each grain has unique microstructure with irregular grain boundaries. These abnormally growing grains were observed by serial sectioning. Each grain had different sectioning thickness. The sectioning thickness of grain A is 2.2μm, that of grain B is 1.6μm and that of grain C is 1.5μm.

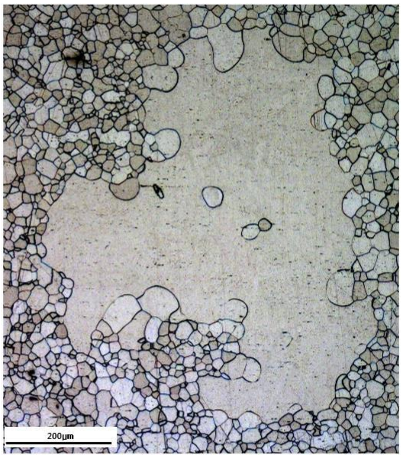

(a)

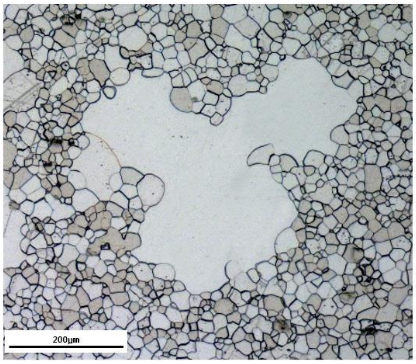

(b)

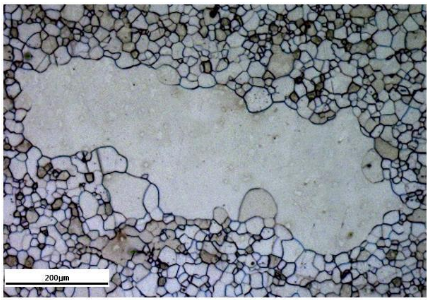

(c)

Figure 4.1 Two-dimensional optical microscopic images of abnormally growing grains (a) A, (b) B and (c) C

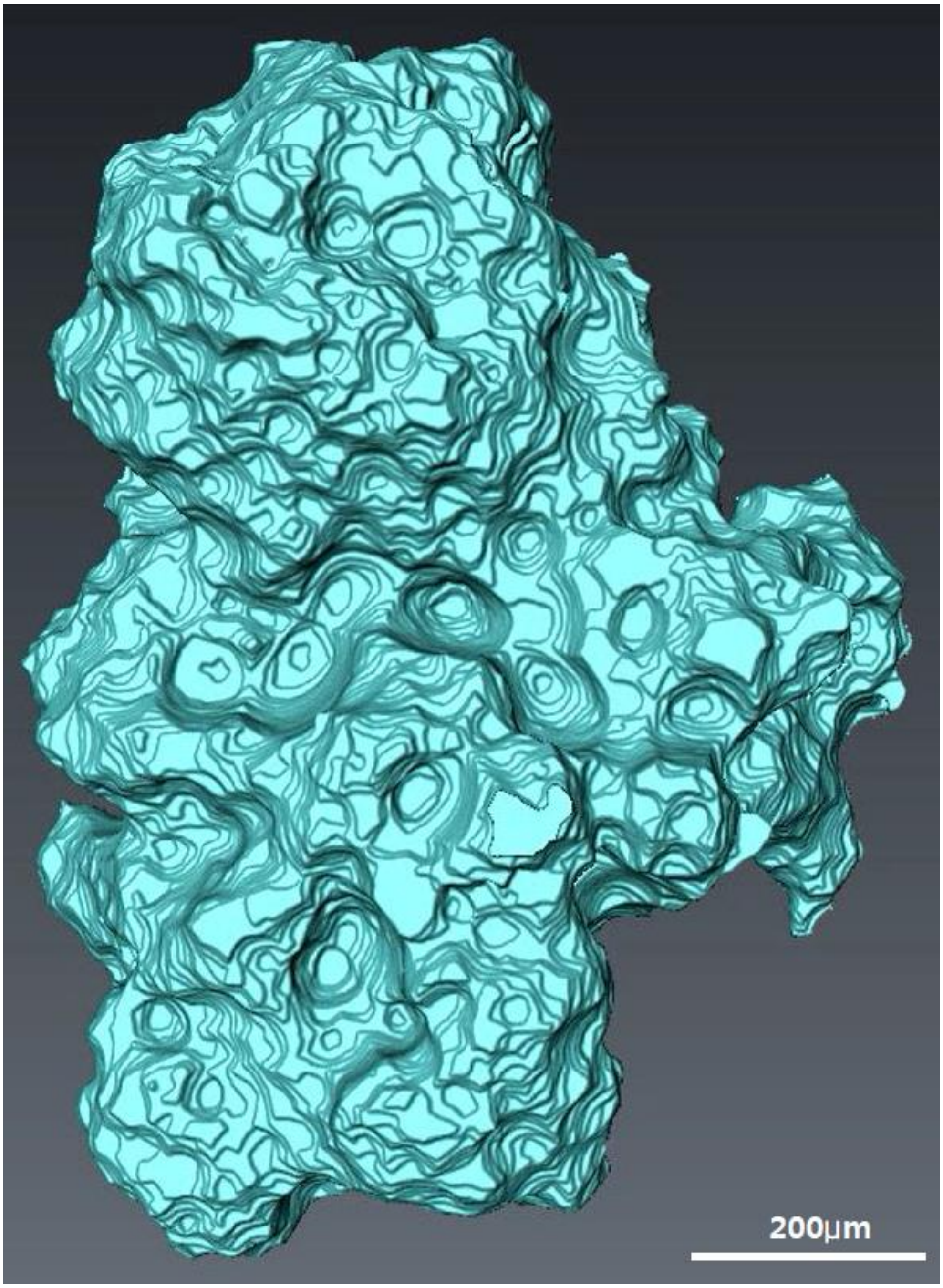

Figure 4.2 Three-dimensional morphology of abnormally growing grain A

To observe the three-dimensional morphology of abnormally growing grains, we reconstructed the grains and eliminate other matrix grains. The three-dimensional morphologies of all grains were reconstructed with about 100 sectioning images with the vertical direction to surface. Figure 4.2, 4.3 and 4.4 is the three-dimensional images reconstructed by the serial sectioned images of abnormally growing grain A. The depth of grain A is about 186μm and the diameter of the grain is about 1mm. These images show that the grain A grow with pancake shape, which means the growth rate in the direction parallel to surface is much higher than in the direction vertical to the surface. Also, the images show that the grain A has extremely irregular boundary shape. Figure 4.5 and 4.6 is the three dimensional morphology of grain B and C and these figures show that grain B and C also have irregular boundary shape.

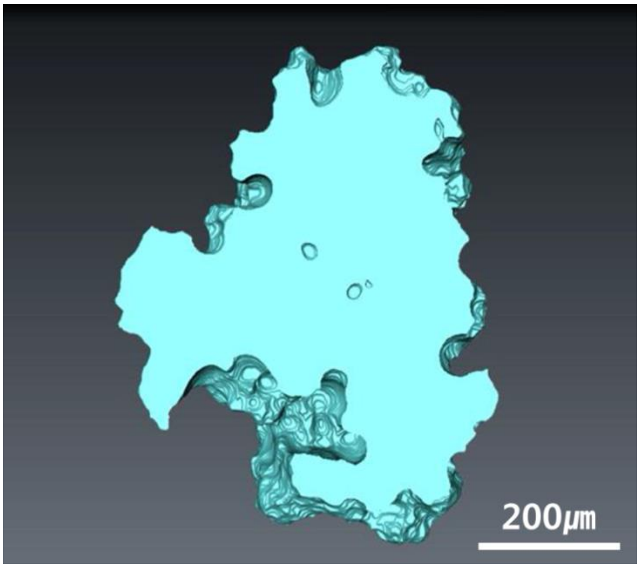

Figure 4.3 Three-dimensional morphology of grain A at the surface

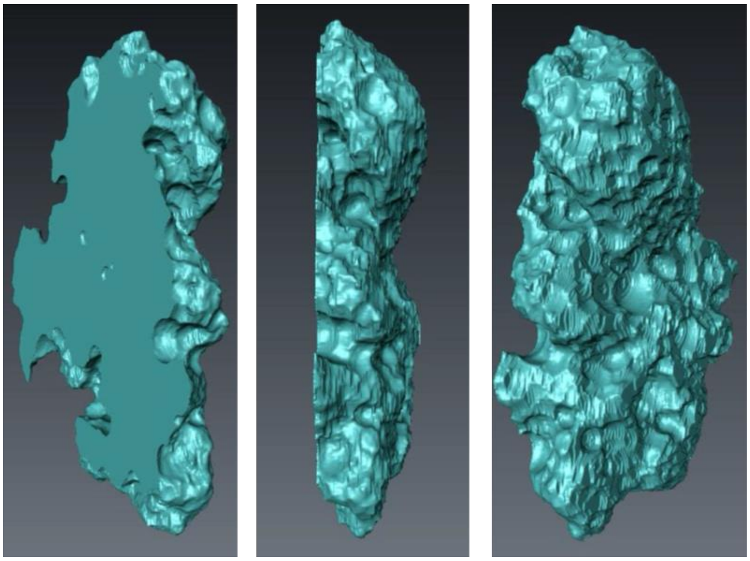

Figure 4.4 Three-dimensional morphology of grain A rotated by (a) 45°, (b) 90° and (c) 135°

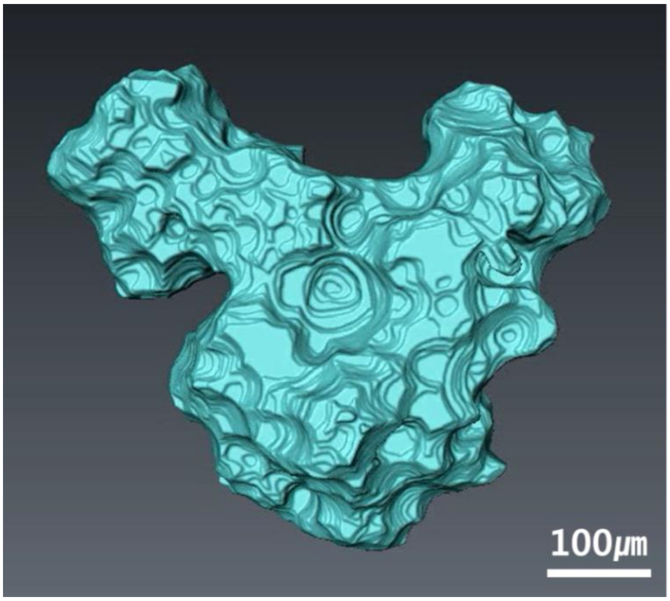

Figure 4.5 Three-dimensional morphology of abnormally growing grain B

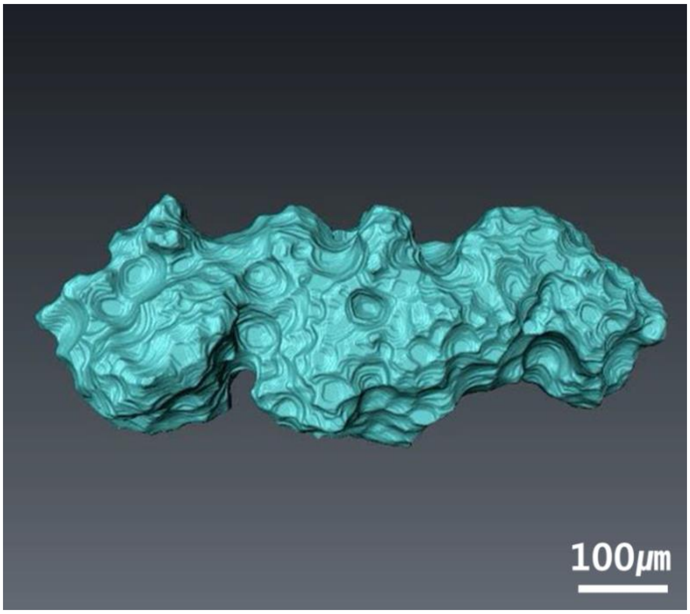

Figure 4.6 Three-dimensional morphology of abnormally growing grain C

There are the typical microstructures of AGG like peninsular grains and island grains. These microstructures observed easily when AGG occurs. Figure 4.7 (a) shows that peninsular grains and island grains exist in the specimen in which grain A grew abnormally. Figure 4.7 (b) shows the three-dimensional morphology of these peninsular grains and island grains near the grain A. Figure 4.7 (b) is the three-dimensional image which presents the specimen consisting of only matrix grains without the abnormally growing grain A. The hollow space at the center of specimen is the place in which the abnormally growing grain A was. From this image the island grain was trapped at the center of the grain A and peninsular grains exist near the grain A.

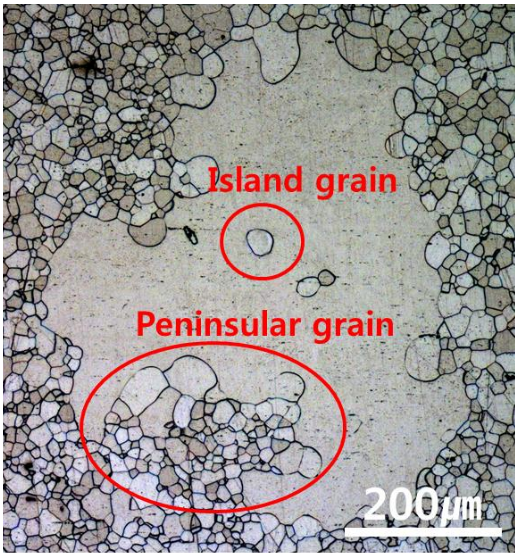

(a)

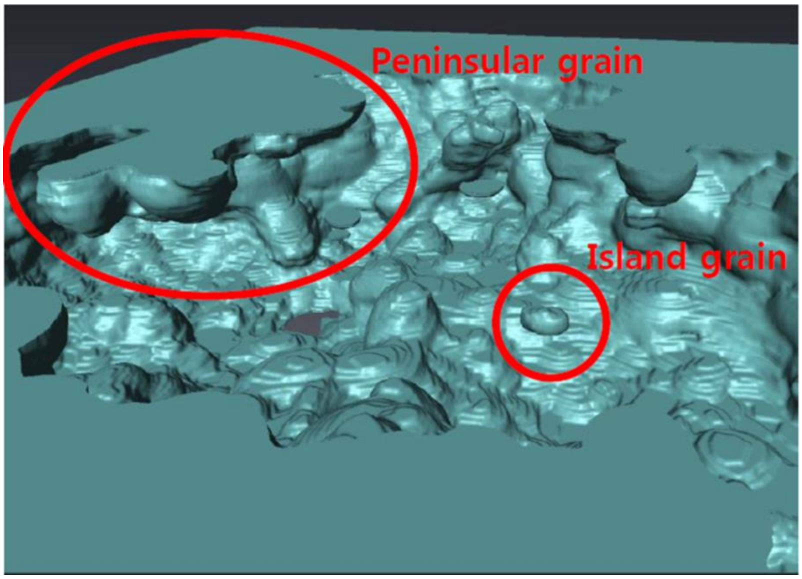

(b)

Figure 4.7 (a) Typical microstructures of AGG (peninsular grains and island grains) (b) three-dimensional morphology of these microstructures

4.3 Similarity of three-dimensional morphology between real Goss grain and simulated Goss grain

Figure 4.8 is the three-dimensional morphologies of normally growing grains obtained by simulation and by serial sectioning. Figure 4.8(a) is obtained by Monte Carlo simulation performed without inhibitors or sub-boundaries. Figure 4.8(b) is a grain in pure iron plate which was annealed at 1000℃ for 2h after cold rolling. Both normally growing grains make facet grain boundaries with neighbor grains.

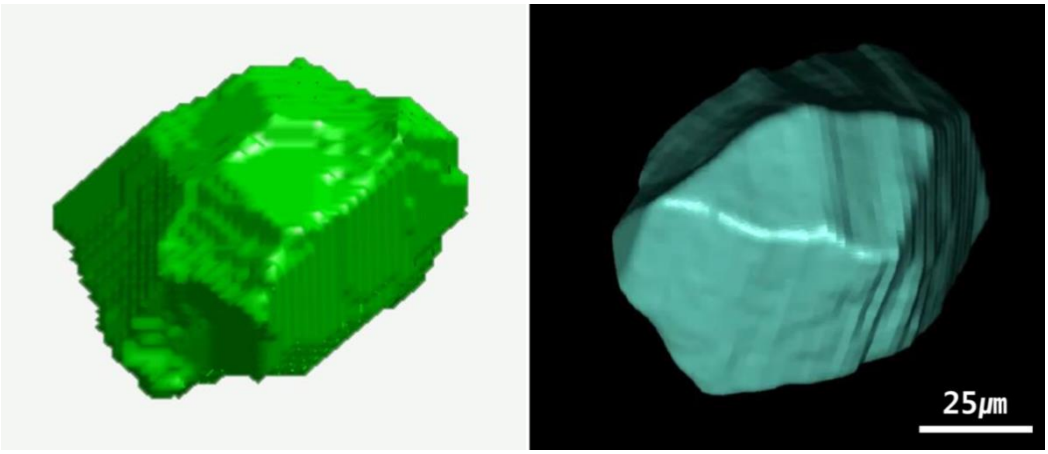

Figure 4.8 Three-dimensional morphology of normally growing grain obtained (a) by simulation and (b) by serial sectioning

Figure 4.9 is the three-dimensional morphologies of abnormally growing grains obtained by simulation and by serial sectioning. Figure 4.9 (a) is the morphology of the abnormally growing grain which is simulated by Monte Carlo simulation performed with real orientations, precipitates and sub-boundaries, which is mentioned at chapter 3. Figure 4.9 (b) is the three-dimensional morphology of the grain A. Both abnormally growing grains have extremely irregular shape and make curved grain boundaries with neighbor grains.

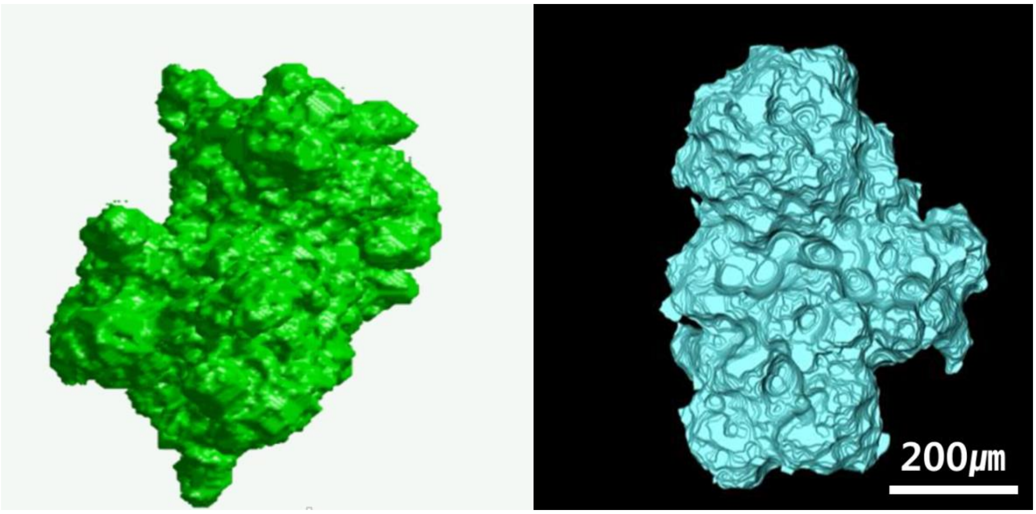

Figure 4.9 Three-dimensional morphology of abnormally growing grain obtained (a) by simulation and (b) by serial sectioning

The simulation, which is mentioned at the chapter 3 and used for the figure 4.8 (a) and 4.9 (a), shows that sub-boundaries and precipitates are necessary for the abnormal grain growth. Because the three-dimensional morphology of the simulated grains is similar to that of the real grains, the simulation was performed realistically and it can be an evidence of sub-boundary enhanced solid-state wetting mechanism.

4.4 Three-dimensional morphological evidence of solid-state wetting

Figure 4.10 is the image of the grain boundaries made by abnormally growing grain A and neighbor matrix grains. Because of force valance, in the three-dimensional image constructed by serial sectioning, the quadruple junction point is presented as a peak. As shown in this figure, there are numerous quadruple junctions at the grain boundaries of abnormally growing grain and quadruple junctions can be identified easily from the three-dimensional image

Figure 4.11 (a) and (b) are the zoom-in image of triple junction line and quadruple junction point. Each quadruple junction is connected with three triple junction line on the grain boundary of the abnormally growing grain. The average length of the triple junction line was 11μm. Figure 4.12 is the quadruple junction point at the surface of reconstructed three-dimensional morphology of abnormally growing grain. The height of this peak is about 11μm which is same the average length of the triple junction lines. This morphology can be made by the quadruple junction wetting along the triple junction line which made by three matrix grains.

Figure 4.10 The surface of reconstructed three-dimensional morphology of abnormally growing grain

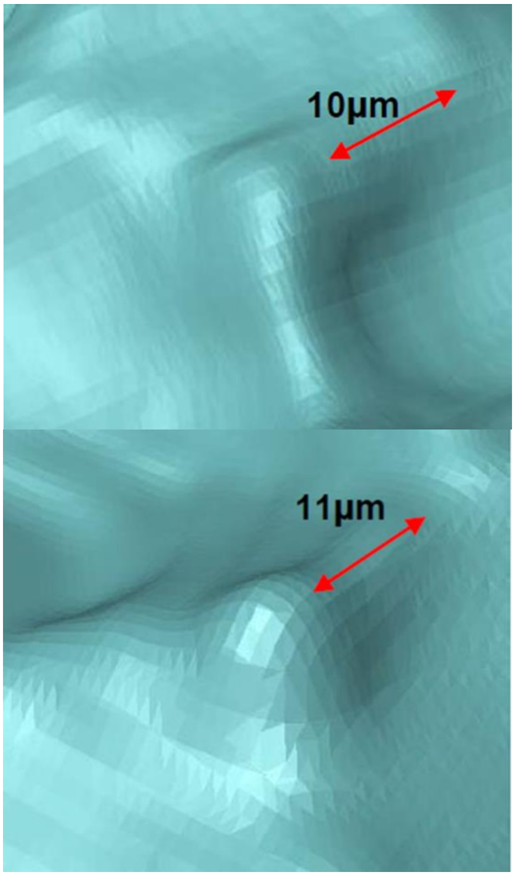

Figure 4.11 The quadruple junction point and the triple junction line at the three-dimensional reconstructed morphology of abnormally growing grain

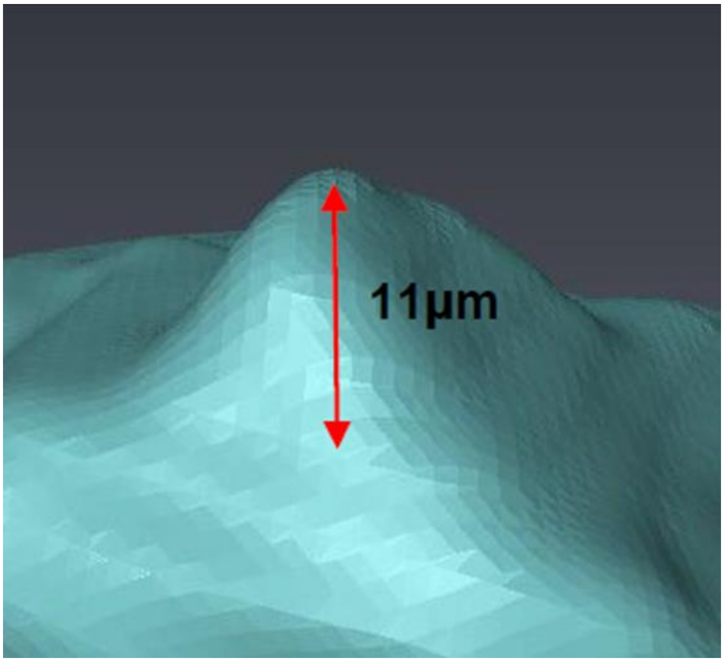

Figure 4.12 The quadruple junction point with the wetting morphology

CHAPTER 5

Three-dimensional simulation for abnormal growth behavior

The three-dimensional simulation performed with sub-boundaries, precipitates and real orientation reproduces the two-dimensional microstructure, the three-dimensional morphology and orientation. Because this simulation reproduces these phenomena well, many typical properties of abnormal grain growth can be understood by this program.

5.1 Effect of sub-boundary energy on abnormal grain growth rate

After secondary recrystallization, the texture is changed to exact Goss texture [7]. Then the abnormally growing grain with large deviation from Goss orientation should be removed during secondary recrystallization. The one way to remove these grains is the rapid growth rate of exact Goss. If the exact Goss grain grows fast, the other grains will be trapped by Goss grain and disappeared. Park et al. proposed that the exact Goss have low stored energy after cold rolling base on FEM simulation [29]. If the exact Goss have lower sub-boundary energy and the abnormally growing grain with lower sub-boundary energy grow faster than other grains, the exact Goss grow faster than other Goss grains and eliminate other Goss grains. This phenomenon is tested by the three-dimensional MC simulation.

As shown in figure 5.1, the two grains are simulated. The green grain A has the sub-boundaries which have the grain boundary energy of 0.01 and the blue grain B has the sub-boundaries whose grain boundary energy is 0.001. Both grains have the Goss orientation. At the initial state, the grain A is bigger than the grain B.

Figure 5.2 is the time evolution of these grains. Figure 5.2 (a), (b), (c), (d), (e) and (f) are the three-dimensional morphologies of the two grains after 0 MCS, 500 MCSs, 1000 MCSs, 1500 MCSs, 2000 MCSs and 2500 MCSs. After 500 MCSs, the size of two grains become similar and the grain B becomes larger than the grain A after 1000 MCSs. Because this simulation uses continuous boundary condition, B grain grows through the left side and appears from the right side. The growth rate of grain B goes faster and surrounds grain A. After 2500 MCSs, the grain A is eliminated by grain B.

This result shows that the sub-boundary energy determines the abnormal grain growth rate and abnormally growing grains with relatively high sub-boundary energies are eliminated by abnormally growing grains with relatively low sub-boundary energies.

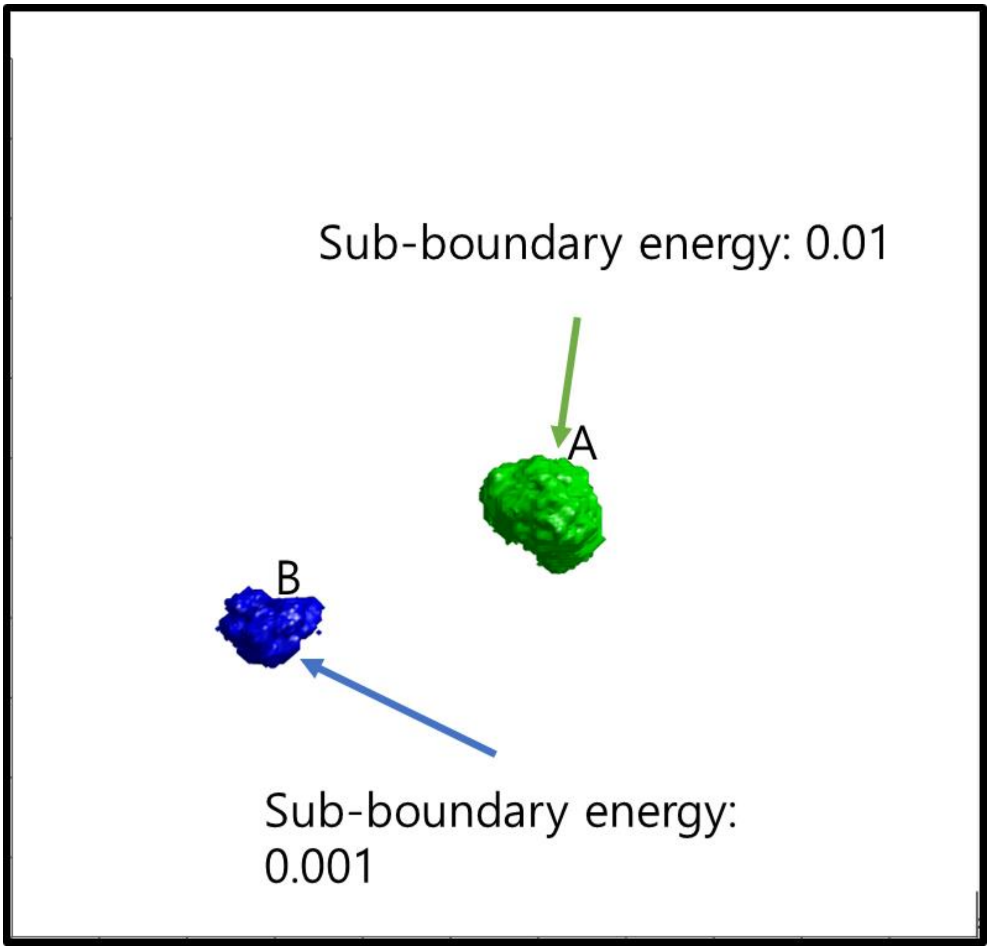

Figure 5.1 Sub-boundary energies of grain A and grain B

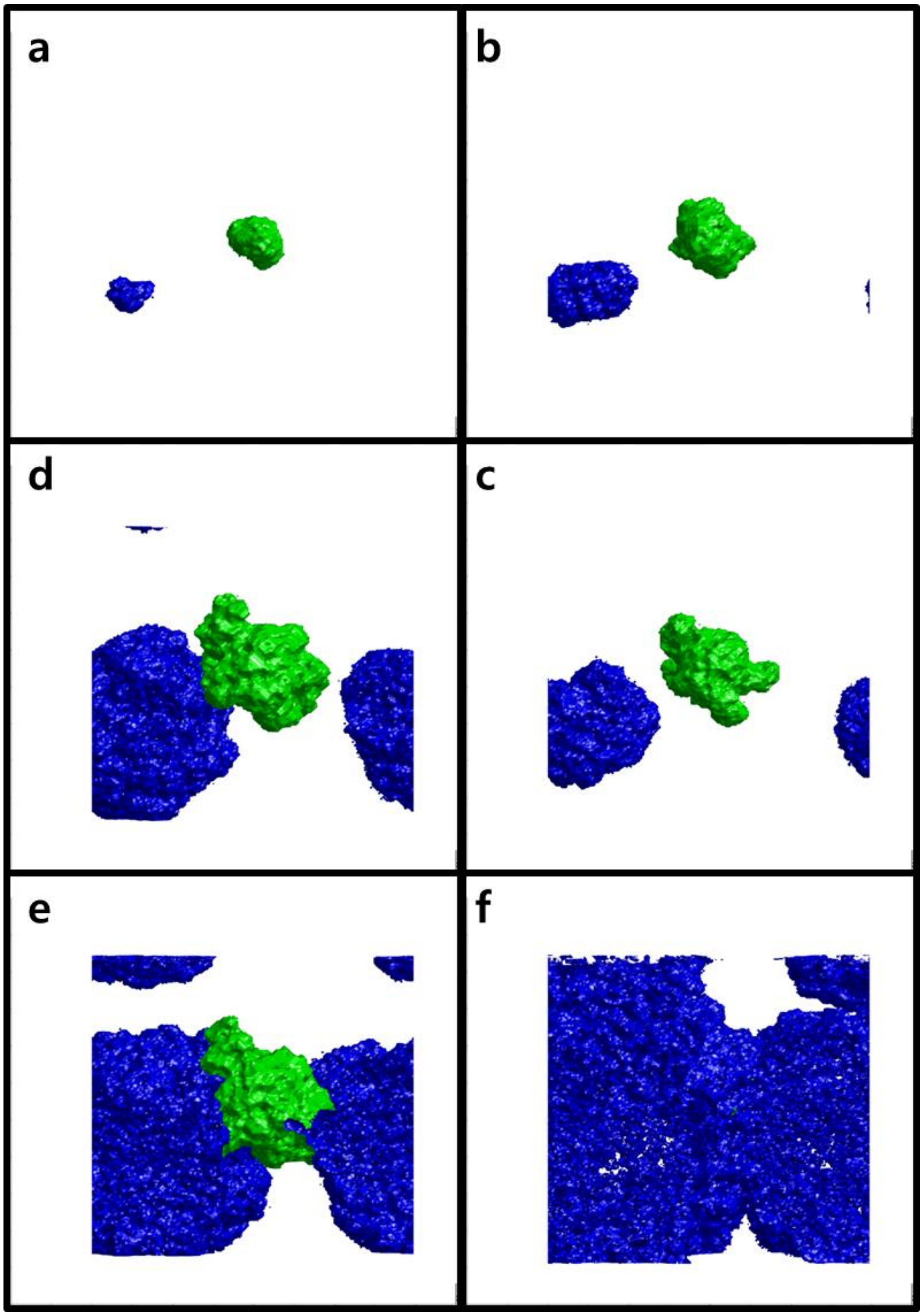

Figure 5.2 Grain growth behavior according to sub-boundary energy

5.2 Effect of texture on abnormal grain growth rate

The second one which can affect abnormal grain growth rate is texture [10]. Abnormal grain growth occurs by sub-boundary enhanced solid-state wetting mechanism. According to the mechanism, wetting probability is determined by the grain boundary energies of penetrated grain boundaries and penetrating grain boundaries. To increase wetting probability, penetrating grain boundaries should have low grain boundary energies and penetrated grain boundaries should have high grain boundary energies. The one of which determine the grain boundary energy is the crystallographic orientation of the two grains exist beside the grain boundary. Therefore, the crystallographic orientation of the matrix grains, texture, can determine the grain boundary energies of penetrated and penetrating grain boundaries. The texture affects grain boundary energy which decide the wetting probability. And the wetting probability decide the abnormal grain growth rate. In the end, the texture affects the abnormal grain growth rate.

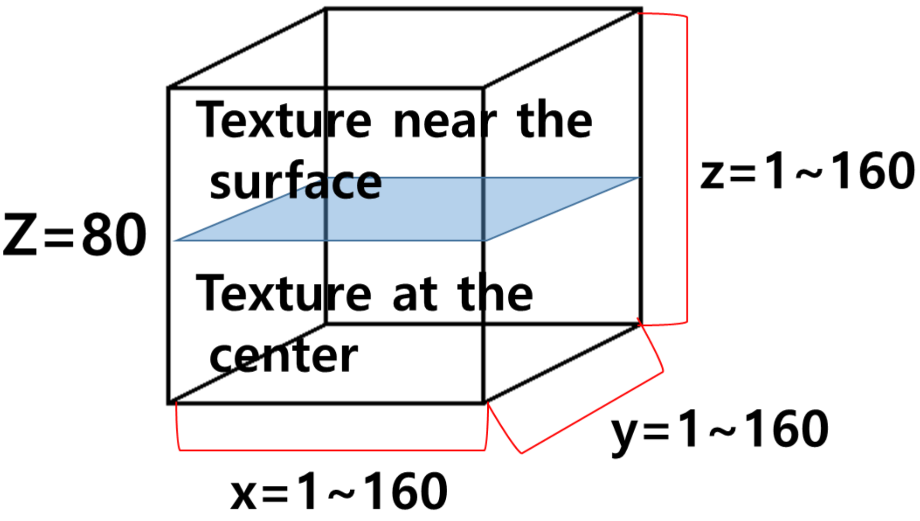

Figure 5.3 Schematics of simulation for texture effects on abnormal grain growth rate; upper side of lattice filled by texture near the surface and lower side of lattice filled by texture at the center

The texture of primary recrystallized Fe-3%Si steel near the surface and that at the center are different. The texture near the surface has more low energy boundary like low angle, Σ5 and Σ9 boundaries than the texture at the center. Then the growth rates of abnormally growing grain in each texture are different from each other. And this is why the abnormally growing grains grow with pancake shape.

To examine that, the three-dimensional MC simulation using two Goss grains with different sub-boundary energies is performed. Figure 5.3 is the schematics of simulation. In the simulation, the grain near the surface is set in upper side of lattice (z>80) and the grain at the center is set in lower side of lattice (z<80). The sub-boundary energy is 0.01.

Figure 5.4 is the three-dimensional morphology of the abnormally growing grain in simulation. Figure 5.4 (a) is the initial state of simulation and figure 5.4 (b) is the state after 5000 MCSs. At the initial state, the abnormally growing grain exist at the center (z=80). After 5000 MCSs, the grain grows faster in the texture near the surface then in the texture at the center.

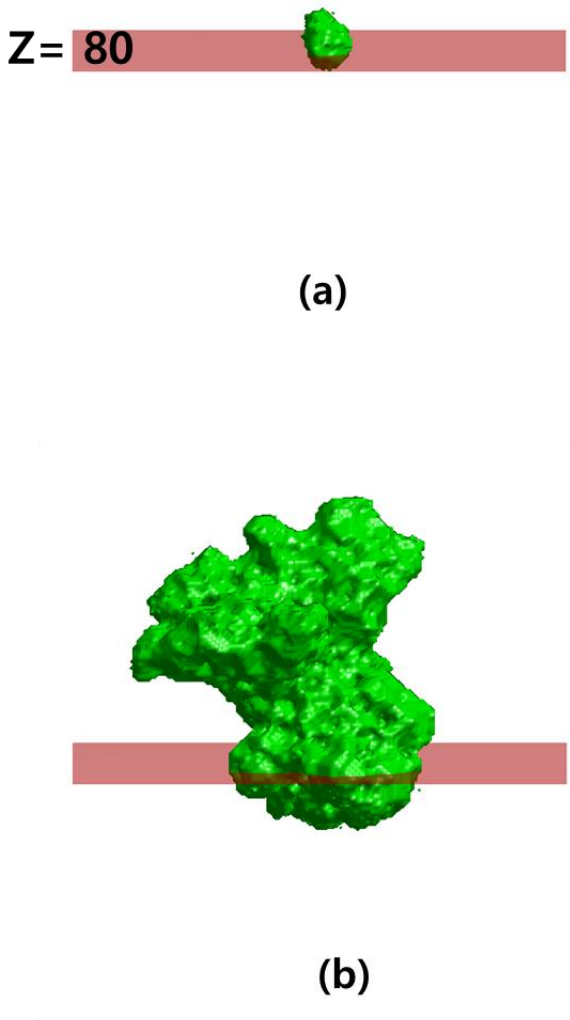

Figure 5.4 the grain growth behavior in the texture near the surface and in the texture at the center; (a) initial state and (b) after 5000 MCSs

The results show that the texture determines the grain boundary energies and the grain boundary energies determine the growth rate of abnormally growing grains. Therefore, the sub-boundary energy and the texture have the key role for the abnormal grain growth rate and it is important to control the sub-boundary energy and the texture.

CHAPTER 6

Improvement in grain-oriented electrical steel by symmetric rolling

6.1 Texture difference between at the surface and at the center

Abnormally-growing grains in Fe-3%Si steel grow much faster in the direction parallel to the surface than in the direction vertical to the surface. This characteristic feature of AGG of Goss grains lead to a pancake shaped growth [52]. Sakai et al. [53] also observed that, during secondary recrystallization, he Goss grains grow in a direction parallel to the surface. These results show that the surface have a growth advantage over the center during secondary recrystallization. From these results, we can predict that the Goss grains favor the texture near the surface after primary recrystallization to grow than that at the center. Homma and Hutchinson [10] confirmed that the texture has an influence on AGG and this result support the prediction.

If this prediction is true, the texture near the surface after primary recrystallization should be different from that at the center. Matsuo et al. [54]

reported such texture inhomogeneity through the thickness after primary recrystallization of Fe-3%Si steel. Park et al. [55] also shows that the texture near surface is different from that at the center and the ratio of grains, which make low energy boundary with Goss grain, especially low angle boundary, $\Sigma5$, and $\Sigma9$ grain boundary, is higher near surface than at the center.

The reason of the texture difference between at the center and near surface is hot rolling. The primary recrystallization texture is affected by the texture before recrystallization. So the texture difference is decided by cold rolling texture because the just previous process of the recrystallization is cold rolling. But during cold rolling, equal strain, plain stress, is applied at the center and near the surface because of lubricant. And cold rolling texture also can be affected by previous texture, hot rolling texture. As a result, the texture difference of primary recrystallization between at the center and near the surface is determined by hot rolling. Mishra et al. observed this phenomenon in the Fe-3%Si steel using X-ray [56].

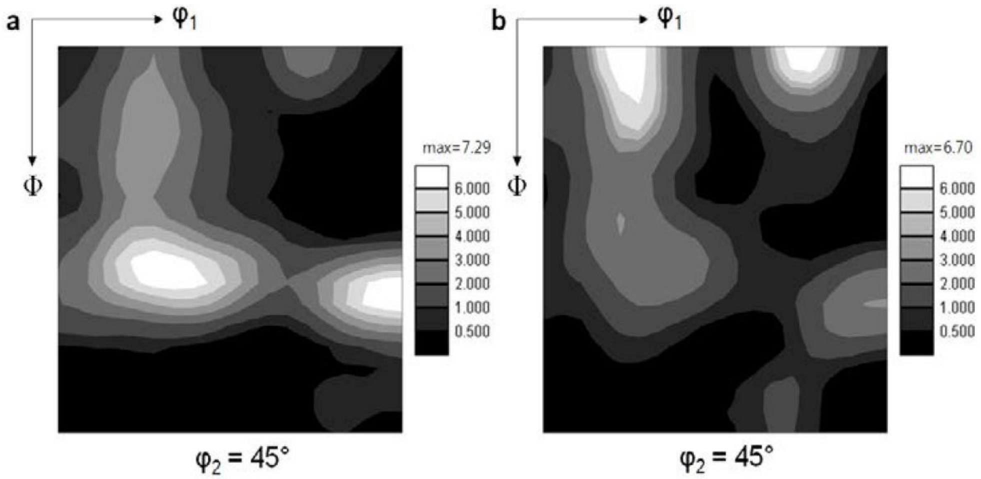

Figure 6.1 ODFs displayed in a $\varphi_2 = 45^o$ at (a) 1/8t and (b) 1/2t, respectively, of the specimens after primary recrystallization [55]

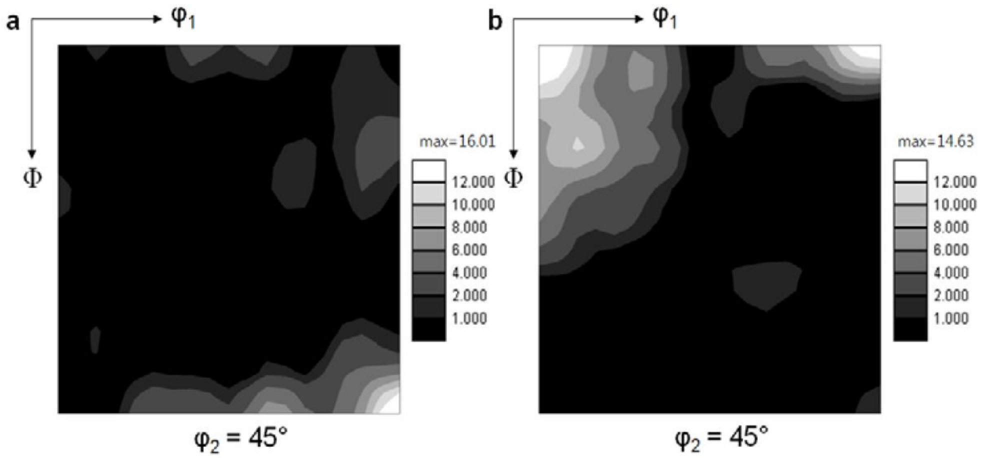

Figure 6.2 ODFs displayed in a $\varphi_2 = 45^o$ at (a) 1/8t and (b) 1/2t, respectively, of the specimens after hot rolling. The Goss texture ($\varphi_1 = 90^o$, $\Phi = 90^o$, $\varphi_2 = 45^o$) was developed at 1/8t whereas the rotated cube ($\varphi_1 = 0^o$, $\Phi = 0^o$, $\varphi_2 = 45^o$) was developed at 1/2t [55]

Figure 6.1 shows that the ODFs displayed in a $\varphi_2 = 45^o$ at 1/8t and 1/2t. As shown in this figure, at the center, rotated cube texture is developed more than γ-fiber texture but near the surface, γ-fiber texture is developed more than rotated cube texture. This texture difference after the primary recrystallization between near the surface and at the center is made by the texture difference after hot rolling between near the surface and at the center. Figure 6.2 is the ODFs displayed in a $\varphi_2 = 45^o$ at 1/8t and 1/2t, respectively, of the specimens after hot rolling. Form this figure, the Goss texture ($\varphi_1 = 90^o$, $\Phi = 90^o$, $\varphi_2 = 45^o$) was developed at 1/8t whereas the rotated cube ($\varphi_1 = 0^o$, $\Phi = 0^o$, $\varphi_2 = 45^o$) was developed at 1/2t. This difference of texture is formed by the difference of dominant strain; shear strain and plane strain are dominant, respectively, near the surface and at the center [57].

The typical crystallographic orientation of the γ-fiber texture is {111}<112> which has the $\Sigma9$ relation with the Goss grain. So it is natural for γ-fiber texture to have the high ratio of the grains which have $\Sigma9$ relation with Goss grains. Figure 6.4 is the ratio of the CSL boundary which is made by the matrix grains with Goss grain. The radio of the CSL boundary, especially $\Sigma1$, $\Sigma5$ and $\Sigma9$, is much higher at 1/8t than at the 1/2t.

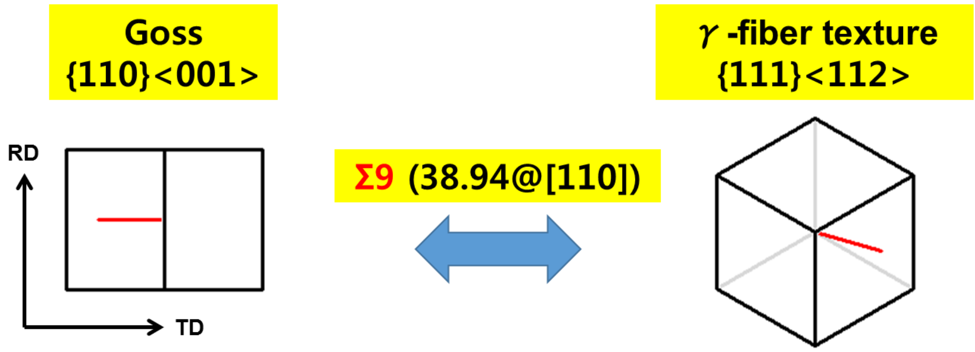

Figure 6.3 The Relation between Σ9 boundary and γ-fiber texture

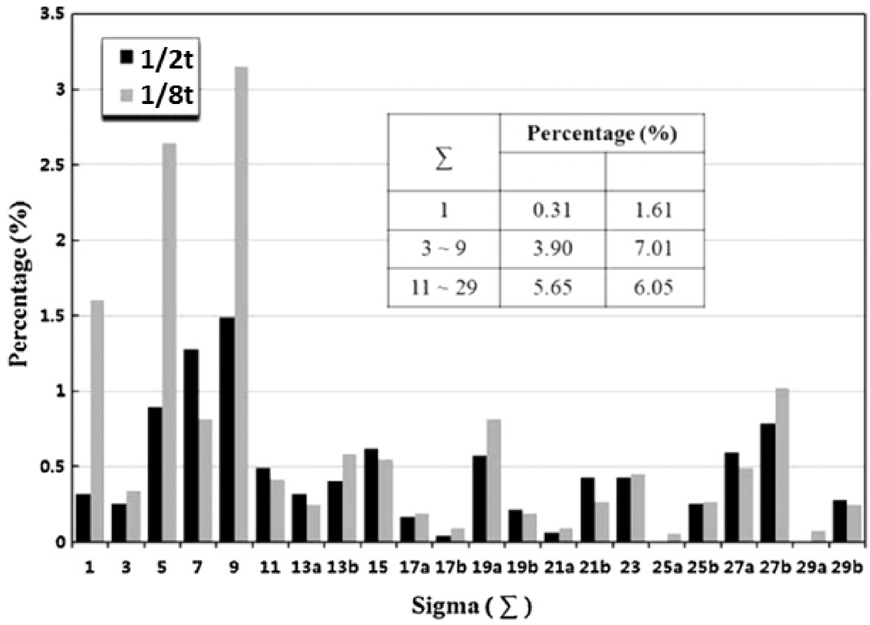

Figure 6.4 The ratio of the CSL boundary between a matrix grain and the Goss grain at the 1/2t and at the 1/8t [55]

As previously mentioned, the texture difference between near the surface and at the center was made by the hot rolling process, Goss grain exist more near the surface than at the center and the texture near the surface has an advantage for the abnormal grain growth. Based on this summary, if the texture at the center can be converted like the texture near the surface than Goss fraction will be increased and the growth rate of the abnormally growing Goss grain will be increased.

To confirm this assumption, asymmetric hot rolling is done. The asymmetric hot rolling is well known as the rolling process which can apply the shear stain in all thicknesses to make the texture at the center like that near the surface [58].

6.2 Experimental procedure

An ingot of Fe-3%Si steel was hot-rolled symmetric to 7.1mm and hot-rolled symmetric and asymmetric to 2.4mm. The later hot-rolling was done at 1150°C by 3 passes like figure 6.5. The reduction of each pass was 30%. Before each step, the sample was heated by the box furnace at 1200°C and the specimens are hot-rolled when the surface temperature reached 1150°C. The asymmetric rolling is done by the different rolling speed between upper and lower rollers. For the symmetric rolling, the rolling speed of all rollers was 20 rpm. In case of the asymmetric rolling, the rolling speed of the upper roller was 24rpm and that of the lower roller was 16 rpm.

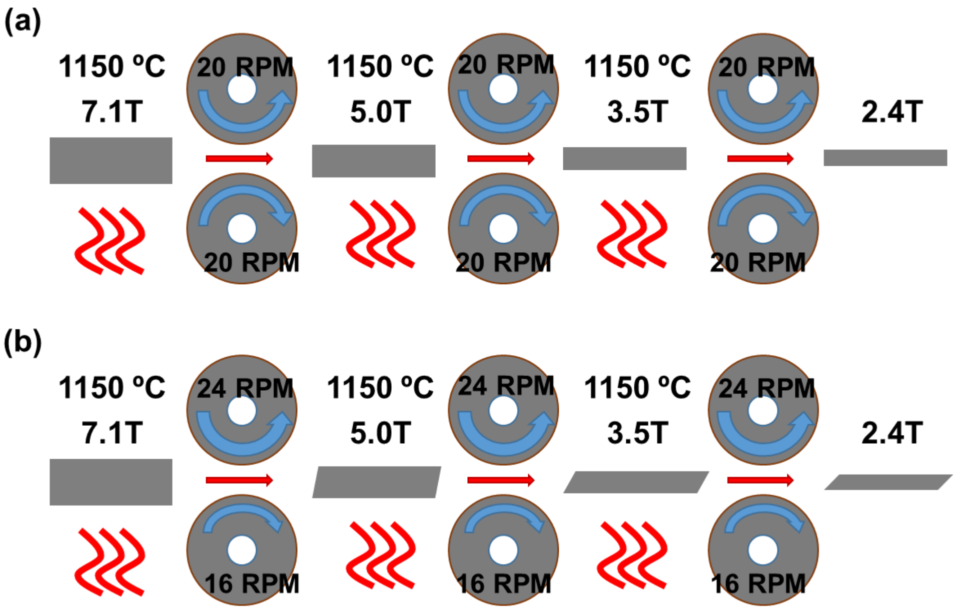

Figure 6.5 Schematic processes of (a) symmetric rolling and (b) asymmetric rolling

The hot-rolled samples were cold-rolled to thickness of 0.3 mm and primary recrystallized at 850°C for 150s in a wet 10% H_2-N_2 atmosphere. The specimens after primary recrystallization were heated in a stepwise fashion at 15°C/h in a 50% H_2-N_2 atmosphere up to 1200°C, held for 0s and cooled to room temperature. The texture of hot-rolled samples as well as primary recrystallization samples were measured by EBSD, attached to a FE-SEM (SU70, Hitachi). EDAX/TSL software was used to determine the texture. ODF with φ_2=45° section was generated using a harmonic series expansion with a series rank 22 with Euler angle representation (φ_1, Φ, φ_2) in Bunge's notation. [59]

The grain size of the secondary recrystallized samples is about ~10 cm so it is impossible to analyze the texture by EBSD. To observe the secondary recrystallization microstructure, the sample was macro etched by 36% HCl soluation at 100℃ for 10~20s.

6.3 Texture of hot-rolled sample produced by asymmetric rolling and symmetric rolling

Figure6.6 is the IPF map of hot-rolled sample to thickness of 7.1mm. This fiugre shows the typical texture of hot-rolled sample. Goss texture is developed near the surface and the rotated cube texture at the center. It is well known that the Goss texture is easily developed when shear stress is applied. Near the surface, the friction between the roll and the specimens makes shear stress. As a result, the Goss texture is developed near the surface. On the other hand, the rotated cube texture is easily developed when plain stress is applied. At the center, the sample does not contact with the roller so there is not friction force and only plain stress is applied. Naturally, the rotated cube texture is developed at the center.

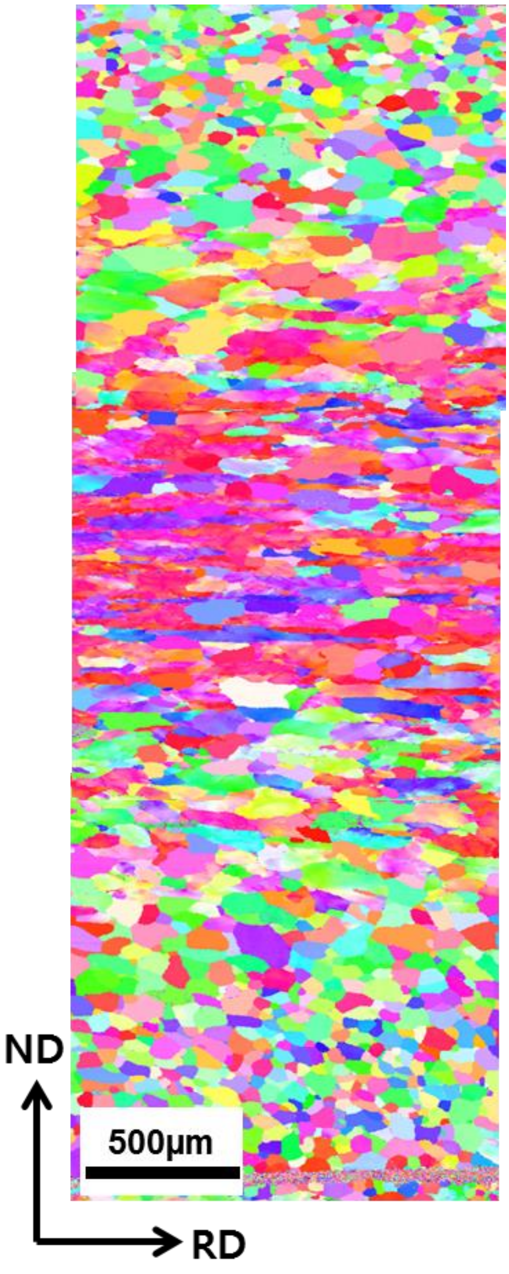

Figure 6.6 The texture of hot-rolled sample to thickness of 7.1mm

Figure 6.7 is the texture of samples which is hot-rolled symetrically and asymmetric. The center part of each samples is indicated by dotted circle. The center part of each sample have different texture. When the sample is hot-rolled symmetric, the texture is similar to that in figure 6.6. At the center, the rotated cube texture is developed and near the surface, the Goss texture is developed. On the other hand, the specimen which is hot-rolled asymmetric the Goss texture is developed in all thickness.

The ODFs of the samples show the more detail information. Figure 6.8 is the ODF of the symmetric and asymmetric hot-rolled samples. Figure 6.8 (a) shows that the symmetric hot-rolled sample has the rotated cube and α-fiber texture which is the typical plain stress texture. And figure 6.8 (b) shows that the copper and Goss texture, the typical shear stress texture, are developed in the sample which is asymmetric hot-rolled. The part indicated by solid line in figure 6.8 (b) shows that the rotated cube texture diappear when the sample is asymmetric hot-rolled. In contrast, the part indicated by dashed line in figure 6.8 (b) shows that the copper texture is developed when the sample is asymmetric hot-rolled.

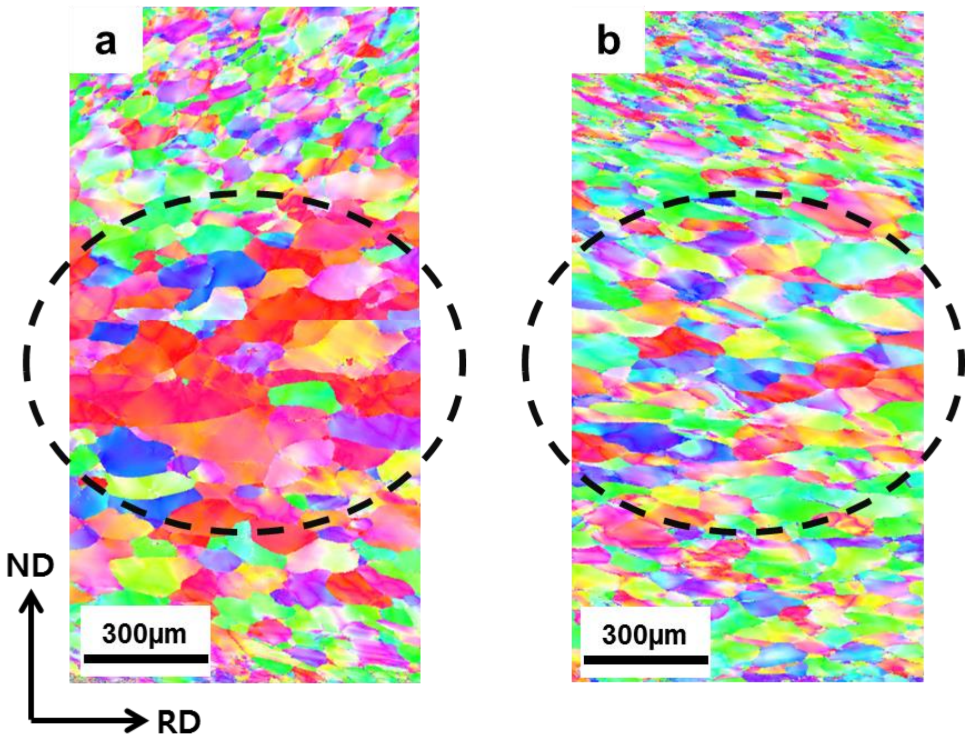

Figure 6.7 The texture of (a) symmetric and (b) asymmetric hot-rolled sample to thickness of 2.4mm

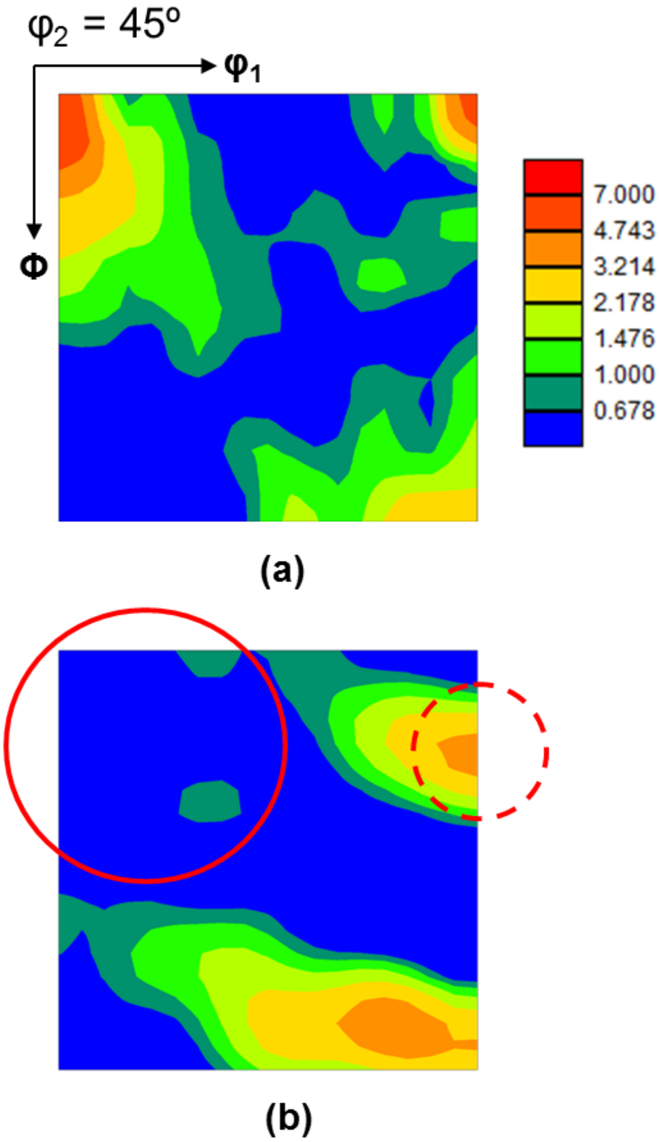

Figure 6.8 The ODFs displayed in a $\varphi_2 = 45^{\circ}$ of (a) symmetric and (b) asymmetric hot-rolled samples to thickness of 2.4mm

The Goss fraction is also changed. Figure 6.9 The symmetric hot-rolled sample have the rotated cube texture at the center so there is not Goss grains at the center. But the texture at the center of the asymmetric hot-rolled sample is not the roated cube texture but the copper and Goss texture. As a result, the asymmetric hot-rolled sample has the Goss grains at its center. The asymmetric hot-rolled sample has higher Goss fraction than the symmetric hot-rolled sample because the place in which the Goss grains exist is larger in the asymmetric hot-rolled sample than in the symmetric hot-rolled sample. The Goss fraction of the symmetric and asymmetric hot-rolled sample is 4.6% and 7.0%, respectively.

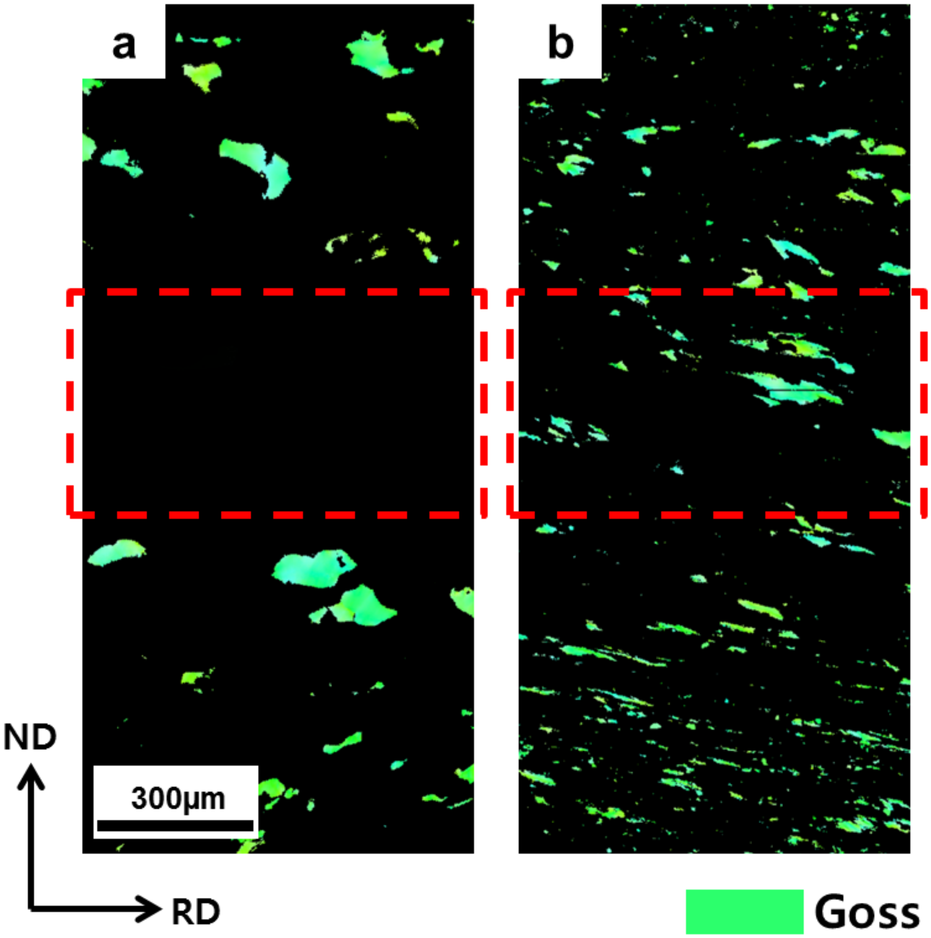

Figure 6.9 The texture of (a) symmetric and (b) asymmetric hot-rolled sample to thickness of 2.4mm

6.4 Texture of 1st and 2nd recrystallized samples produced by asymmetric rolling and symmetric rolling

Figure 6.10 is the ODFs displayed in a φ_2 = 45° of the primary recrystallized sample. Figure 6.10 (a) and (b) are the ODF of the symmetric hot-rolled sample after primary recrystallization at the center (1/2t) and near the surface (1/8t), respectively. The center of the symmetric hot-rolled sample has stronger {100}<021> texture and weaker γ-fiber texture than the part at 1/8t of the sample. Figure 6.10 (c) shows that the asymmetric hot-rolled sample has the similar texture at the center with that of symmetric hot-rolled sample near the surface. By asymmetric rolling, the γ-fiber and α*-fiber texture become, respectively, stronger and weaker. From this result, it is confirmed that the texture of the hot-rolled specimen effects on the texture of the primary recrystallized one.

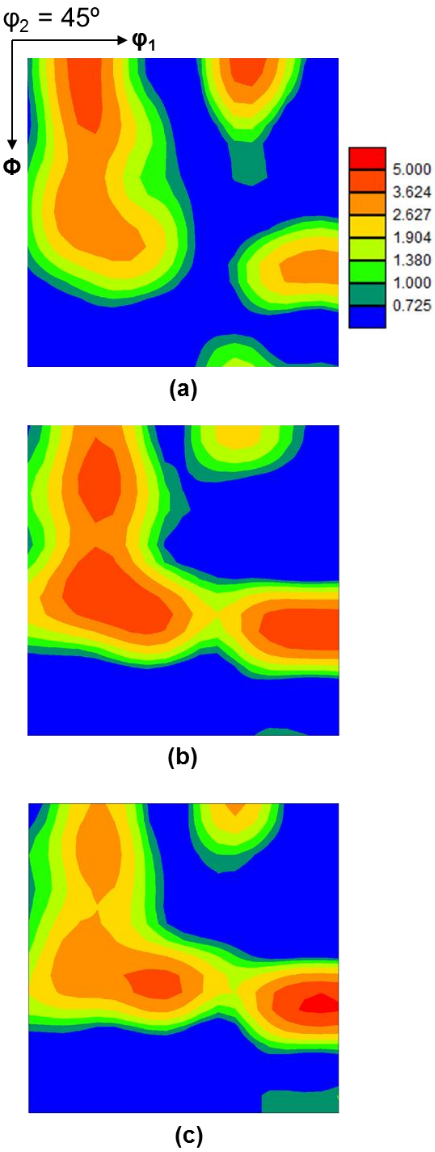

Figure 6.10 The ODFs displayed in a φ_2 = 45° of the primary recrystallized sample; (a) symmetric hot-rolled sample at the center and (b) at the surface and (c) asymmetric hot-rolled sample at the center

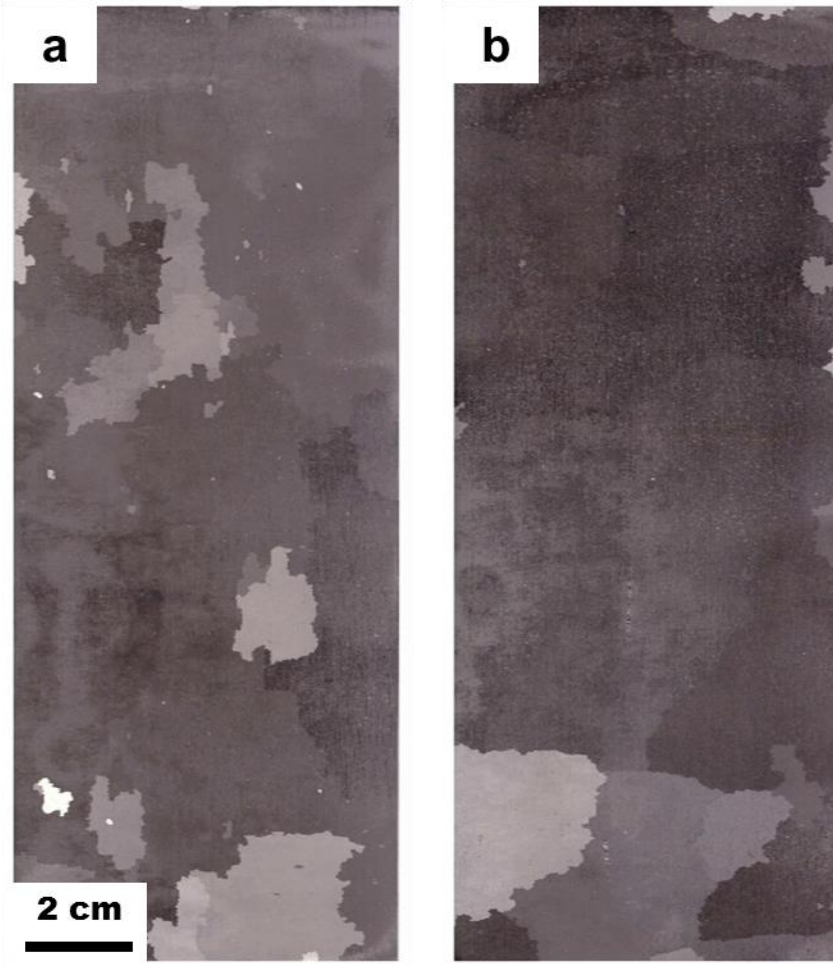

Figure 6.11 The macro etched image of (a) symmetric and (b) asymmetric hot-rolled sample after the secondary recrystallization

The figure 6.11 is the macro etched sample after the secondary recrystallization. The grain size after the secondary recrystallization is bigger in the asymmetric hot-rolled sample than the symmetric hot-rolled sample. The number of the small grains in the asymmetric hot-rolled sample is smaller than that in the symmetric hot-rolled sample. Also, the magnetic property is improved because of these differences. Magnetic flux density (B10) and magnetic core loss (W17/50) of the symmetric rolled sample after the secondary recrystallization are respectively 1.85T and 1.42 W/kg. Magnetic flux density (B10) and magnetic core loss (W17/50) of the symmetric rolled sample after the secondary recrystallization are respectively 1.91T and 1.16 W/kg. The asymmetric hot-rolling increases magnetic flux density and decreases magnetic core loss after the secondary recrystallization. As a result, we can improve the magnetic properties of the grain-oriented electrical steel by asymmetric rolling.

CHAPTER 7

Conclusion

Based on the sub-boundary enhanced solid-state wetting mechanism for AGG in metallic system, grain boundaries and morphology of abnormally growing grains are researched, the MC simulation for abnormally growing grains are performed and the magnetic properties of grain-oriented electrical steel is improved.

The growth front of the abnormally growing grains in Al 5052 alloy was observed and analyzed by EBSD, focusing on the penetration morphology. The grain boundary energies estimated from the misorientation data satisfy the energetic condition for the triple junction wetting. Some grains, which look separate from the abnormally growing grain, were found to have the identical orientation with abnormally growing grain. Through serial section images of these microstructures, it was shown that these grains are the growth front of the abnormally growing grain, which proceeds by wetting along the triple junction line. These results, combined with the recent findings that sub-boundaries exist exclusively in abnormally growing grains, provide the strong evidence for the mechanism of sub-boundary enhanced solid-state wetting for AGG.

To understand the mechanism of abnormal grain growth based on the mechanism of sub-boundary enhanced solid-state wetting, the parallel MC simulation using the real primary recrystallization orientation of Fe-3%Si steel was performed with precipitates and sub-boundary on the abnormally growing grain. The simulation shows that the precipitates maintain the fraction of the high energy boundaries between matrix grains by grain growth inhibition and maintain the probability of wetting. It also shows that the low energy of the sub-boundary increases the probability of wetting. Because of this, precipitates and sub-boundary is necessary to enhance AGG.

If the simulation is based on the proper mechanism, the simulation reproduces all features of AGG. The simulation with the real orientation, precipitates and sub-boundaries reproduced the typical features of AGG such as the island and peninsular grains and merging of abnormally growing grains, appearing separate on the two-dimensional image. And the three-dimensional morphology of simulation is also analyzed. The three-dimensional morphology of simulation is extremely irregular and similar to that of a real abnormally growing grain reconstructed by serial section.

The three-dimensional morphology of an abnormally growing grain reconstructed by serial sectioning is analyzed. The three-dimensional morphology of the abnormally growing grains are extremely various like the simulation. The grain boundaries of the abnormally growing grains were extremely irregular as the simulated grain boundaries and the wetting morphologies were observed.

By the simulation, the sub-boundary energies and the texture effects on the abnormal grain growth rate are analyzed. According to simulation, lower sub-boundary make the abnormal grain growth rate faster. And the texture which makes low grain boundary energy with Goss grain make the abnormal grain growth rate fast.

These observations and analysis show that sub-boundary enhanced solid-state wetting is the mechanism of abnormal grain growth. According to the previous result, the primary recrystallization texture effects on the abnormal grain growth rate. Normally, the texture at the center is different from that near the surface. And because the texture near the surface has an advantage for abnormal grain growth, the abnormally growing grain has a pancake shape. By asymmetric rolling, the texture at the center is changed as the texture near the surface and the magnetic properties of the grain-oriented electrical steel is improved.

Chapter 8

Parallel Monte-Carlo simulations for the effect of precipitates and sub-boundaries on abnormal grain growth in Fe-3%Si steel

This part was published in Philosophical Magazine 93 (2013) 4198-4212 and I was the co-author of this paper

This chapter describes for the effect of precipitates and sub-boundaries on abnormal grain growth using parallel three-dimensional Monte-Carlo method based on the real orientation data in Fe-3%Si steel. Especially, we were focused on comparison of the microstructure evolutions between simulation and experimental results. In the other part, three-dimensional morphologies of abnormally-growing grains were analyzed using simulation data.

8.1 Introduction

Previously, many studies have demonstrated using computer simulations that AGG could be happened only if NGG of matrix grains is inhibited by second-phase particles [30, 60, 61] [62]. Our group also reported the three-dimensional MC simulations to examine the effect of precipitates and sub-boundaries on AGG based on the mechanism of sub-boundary enhanced solid-state wetting [63]. Although these studies showed that precipitates played a critical role in inducing AGG, the orientations of initial grains for simulation were randomly chosen, not based on the real orientation data. Also, the grain boundary energy to be proportional to the difference between the orientation numbers of two adjacent grains. Because of these non-realistic assumptions, the simulation results could not reproduce some realistic features of AGG.

The purpose of this study is to examine the effect of precipitates and sub-boundaries on the Goss AGG based on the real texture obtained after primary recrystallization of Fe-3%Si steel and also based on the realistic grain boundary energy determined as a function of the misorientation between two adjacent grains using theoretical and experimental relations. The simulations were compared with the experimental features of AGG.

8.2 Implementation of simulation conditions

MC simulation for 3-D grain growth was performed on a simple cubic lattice using a method similar to that reported by Ko et al [21]. The lattice has 160x160x160 sites with periodic boundary conditions. These sites will be represented by the (x, y, z) Cartesian coordinates in the display. Each site with its own number, Si, represents the crystallographic orientation at the specific location so that surrounded adjacent sites with the same number are the same grain and the sites with different numbers belongs to other grains. The orientation number, Si, is assigned with a set of Euler angles (φ1, Φ, φ2).

The misorientation angle between two adjacent grains can be calculated from Euler angles [64]. Since a cubic lattice has 24 symmetries, one set of Euler angles has 24 matrixes of directional cosines. The matrix multiplication of two Euler angles of adjacent grains produces 24 x 24 matrixes, among which the matrix with the minimum angle corresponds to the misorientation angle of adjacent grains. The grain boundary energy is determined from the misorientation angle by the following equations derived by Read and Shockley [33].

$$J(S_i, S_j) = \begin{cases} \frac{\theta}{\theta_{RS}}\left[1 - \ln\left(\frac{\theta}{\theta_{RS}}\right)\right], & \theta < \theta_{RS} \quad (low\ angle\ boundary) \\ r', & \theta \geq \theta_{RS} \quad (high\ angle\ boundary) \end{cases} \tag{8.1}$$

where J(Si, Sj) is the energy between orientations S_i and S_j, θ is the misorientation angle, θ_{RS} is assigned to be 15° as the high misorientation angle cut-off, and r' is a random value in the range 1.0 - 1.4 for an energy variation. The energy sum between a given site and its first, second and third nearest neighbours is given by the following equation:

$$E = \sum_{nn} J(S_i, S_j)[1 - \delta_{ij}] \quad (8.2)$$

where *nn* is the number of nearest neighbours and δ_{ij} is the Kronecker delta function. The sum is taken over all nearest neighbour sites: 26 up to the third nearest neighbours in the simple cubic lattice. A lattice site is selected at random and a candidate site for energy comparison is chosen from the 26 nearest neighbours. The energy given by equation (8.2) is compared between the two sites and if the energy change is zero or negative, the new orientation of the neighbour is accepted. If the energy change is positive, the new orientation is accepted by the Boltzmann probability, P, given

$$P = \exp(-\Delta E / k_B T) \quad (8.3)$$

where ΔE is the energy change due to the orientation change, k_B is the Boltzmann constant and T is the lattice temperature, which is carefully chosen to avoid both lattice pinning and disordering of boundaries [65].

The 3-D MC simulation of grain growth in this study was performed in parallel computing by using open multi-processing [66], parallel machines with Intel Core i7 (TM) CPU 2.80 GHz and the compiler of Intel Parallel Studio XE 2011. An attempt to reorient the 1603 lattices is referred to as one Monte Carlo step (MCS) and typical simulations were performed until 15000 MCS. The simulation data were converted into the format for the TSL/EDAX, which displayed the texture plots and grain growth.

The initial microstructure consists of 8,000 grains with a uniform grain size and grain boundaries with the same mobility. Also, this microstructure has a texture that is very similar to the real texture, which was acquired from the orientation image mapping by EBSD on 1/8 depth surface of a primary recrystallized Fe-3%Si steel. The specimen was prepared by the standard processing. Figure 8.1(a) and (b) show the $\varphi 2$-section images of orientation distribution function (ODF) of the real microstructure of the Fe-3%Si steel and the initial microstructure of MC simulations, respectively. These are not much different from a typical texture of primary recrystallized Fe-3%Si steel reported previously [10, 67]. The Goss grain is composed of eight sub-grains with the sub-boundary energy of 0.05 based on the experimental observation in Fe-3%Si steel by Park et al [22].

CSL boundary distributions between Goss and matrix grains of the initial microstructure for the MC simulation were calculated and compared with the experimental data in Figure 8.2. The CSL distributions of the initial microstructure are in good agreement with the experimentally-determined CSL distribution. For example, the percentage of $\Sigma 9$ boundaries is slightly higher than those for other CSL types [8]. 16% of all grain boundaries between Goss and matrix grains in the initial microstructure are of a low angle ($\theta<15°$) or CSL. The CSL boundaries are determined with the Brandon criterion, $v_m = \theta_{RS}/\Sigma^{1/2}$ [34], and the energy of CSL boundaries up to Σ33 is assumed to be low. The energy variation of a CSL boundary, when deviating from the exact CSL angle, is based on the Read-Shockley function as reported by Ko et al [21].

$$J = \frac{w}{v_m}\left[1 - \ln\left(\frac{w}{v_m}\right)\right], \qquad \frac{w}{v_m} < 1 \tag{8.4}$$

where w is the deviation from the exact CSL angle. The minimum energy of a CSL boundary is limited to be 0.3. The energy range was determined from the mesoscale grain growth simulations considering the grain boundary misorientation and inclination in iron [35].

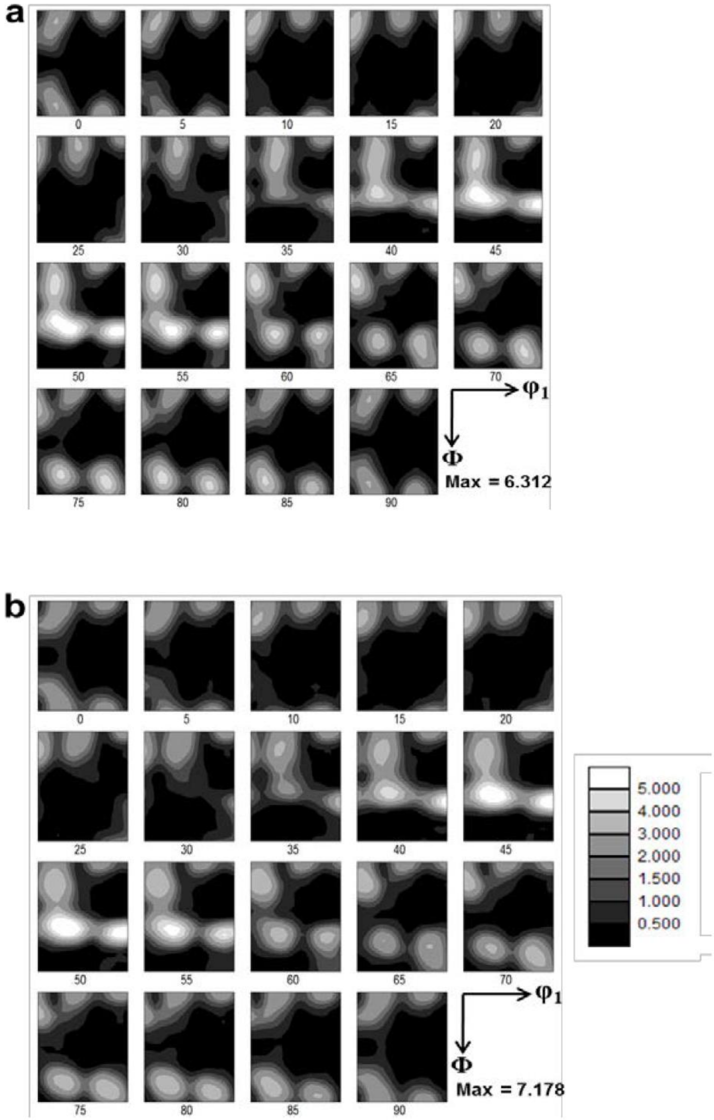

Figure 8.1 φ2-section images of ODF plot from (a) the experimentally-observed texture in 1/8 depth of primary recrystallized Fe-3%Si steel and (b) the texture input for the initial microstructure of simulations.

.

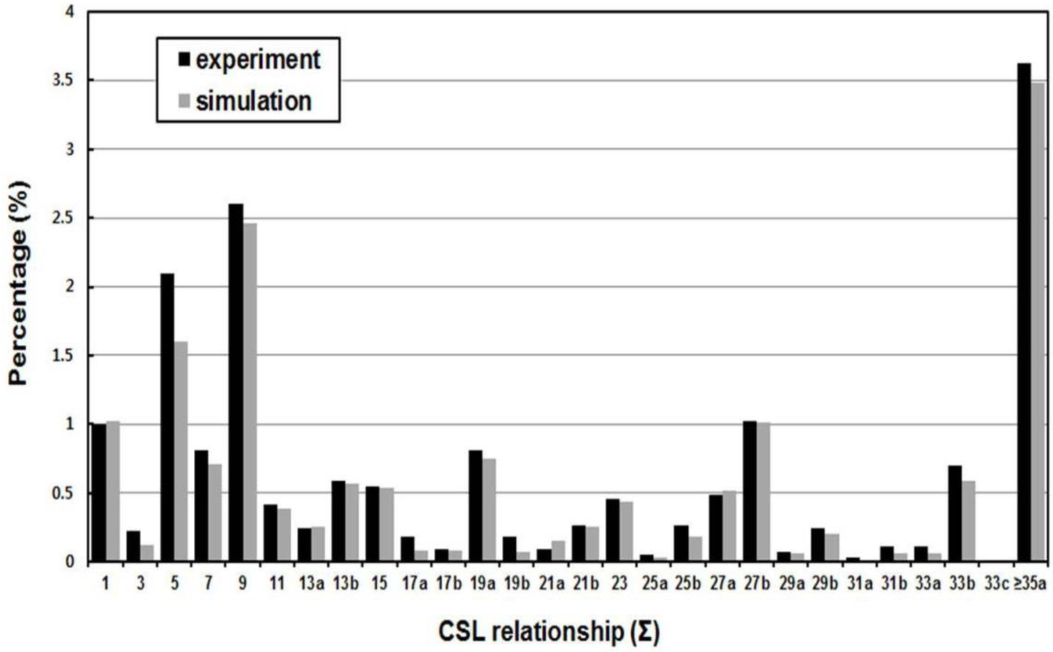

Figure 8.2 Comparison of the CSL boundary distributions between Goss and matrix grains between the experimentally-observed texture (black bar) and the simulation texture (grey bar).

8.3 Simulation results

8.3.1 The role of precipitates in abnormal grain growth

In order to examine how the precipitates affect the AGG behavior, the MC simulations were compared between the conditions with and without precipitates. Figure 8.3(a), (b) and (c) show the cross-section (x, y) images of a 3-D microstructure at z = 80, respectively, after 500, 1000 and 1500 MCS without precipitates. The white grain contains sub-boundaries, which are represented by the black lines. In the early stage before 500 MCS (Figure 8.3(a)), the white grain grew rapidly compared with other grains. After 1500 MCS (Figure 8.3(c)), however, the white grain did not grow faster than some matrix grains. This means that the white grain cannot grow abnormally without precipitates.

In the presence of precipitates, however, the white grain grew abnormally as shown in Figure 8.4. Figure 8.4(a), (b) and (c) show the cross-section (x, y) images of a 3-D microstructure at z = 80, respectively, after 5000, 10000 and 15000 MCS with precipitates. It should be noted that the MCS values in Figure 8.4(a), (b) and (c) are larger than those of Figure 8.3(a), (b) and (c), respectively, by 10 times. This is because the overall growth rate of matrix grains in Figure 8.4, where the grain growth is inhibited by precipitates, is much lower than that in Figure 8.3. The initial conditions in Figures 8.3 and 8.4 were the same including the misorientation distribution of matrix grains. In contrast with the white grain in Figure 8.3, which grew relatively fast in the initial stage and then relatively slowly in the later stage, the white grain

in Figure 8.4 grew faster and faster with simulation time, which is typical of the AGG behaviour. After 15000 MCS in Figure 8.4(c), the white grain becomes 332 times larger than the average size of matrix grains. Therefore, Figures 8.3 and 8.4 clearly reveal the role of precipitates in inducing AGG from the viewpoint of sub-boundary enhanced solid-state wetting.

Then, why do the precipitates enhance AGG? Without precipitates, the grain growth is not inhibited and the matrix grains grow extensively as shown in Figure 8.3. It should be noted that the grain growth not only increases the average grain size but also decreases the fraction of high energy boundaries and increases the fraction of the low energy boundaries when the grain boundary energy is anisotropic [68]. Considering the condition of triple junction wetting derived by Park et al. [31] in the presence of sub-boundaries, the wetting probability is increased with increasing fraction of the high energy boundaries between matrix grains. Therefore, the probability would decrease markedly when the fraction of the high energy boundaries decreases by extensive grain growth and the sub-boundary enhanced solid-state wetting would not occur frequently enough to induce AGG. In the presence of precipitates, however, the grain growth of matrix grains is inhibited markedly as shown in Figure 8.4. Therefore, the fraction of high energy boundaries is maintained to be relatively high, which would increase the wetting probability high enough to induce AGG.

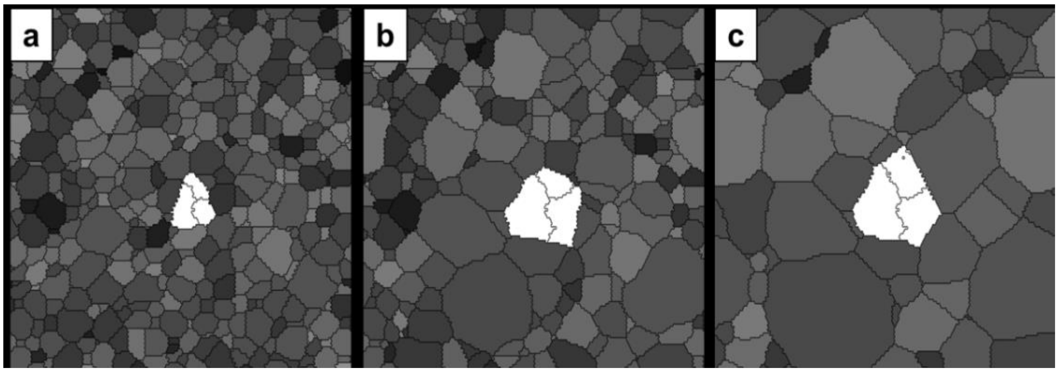

Figure 8.3 Cross-sections (x, y) of the 3-D microstructure at z = 80 in the absence of precipitates after (a) 500, (b) 1000 and (c) 1500 MCS. The white grain has a Goss orientation and black lines inside the white grain indicate sub-boundaries with the energy of 0.05

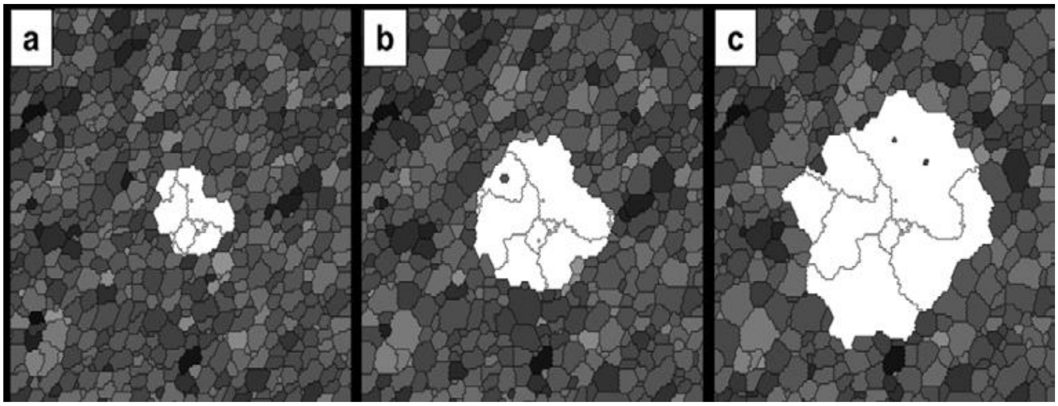

Figure 8.4 Cross-sections (x, y) of the 3-D microstructure at z = 80 in the presence of precipitates after (a) 5000, (b) 10000 and (c) 15000

MCS

This aspect of the percentage change of the low energy boundaries such as low angle and CSL boundaries among matrix grains is shown clearly in Figure 8.5(a) and (b), respectively, for the cases without and with precipitates. Σ values were calculated from the low angle misorientation ($\Sigma1$) to $\Sigma11$ because the low energy for special boundaries was considered up to $\Sigma11$ in the MC simulation. In Figure 8.5(a) for the MC simulation without precipitates, the percentage of low energy boundaries, which are low angle and CSL boundaries, changed noticeably, increasing from the initial value (0 MCS) of 18.8% to 23.4%, 28.1% and 37.5%, respectively, after 500, 1000 and 1500 MCS. The percentage of low energy boundaries after 1500 MCS became twice larger than that in the initial microstructure. On the other hand, in Figure 8.5(b) for the MC simulation with precipitates, the percentage changed only a little, increasing from the initial value of 18.8% to 19.2%, 19.8%, and 22.0%, respectively, after 5000, 10000, and 15000 MCS. It should be noted that the percentage of low angle boundaries shared by Goss grains (Figure 8.2) is about 10 times less than that between matrix grains (Figure 8.5). This is because a strong γ-fiber texture is evolved after primary recrystallization of Fe-3%Si steel [10].

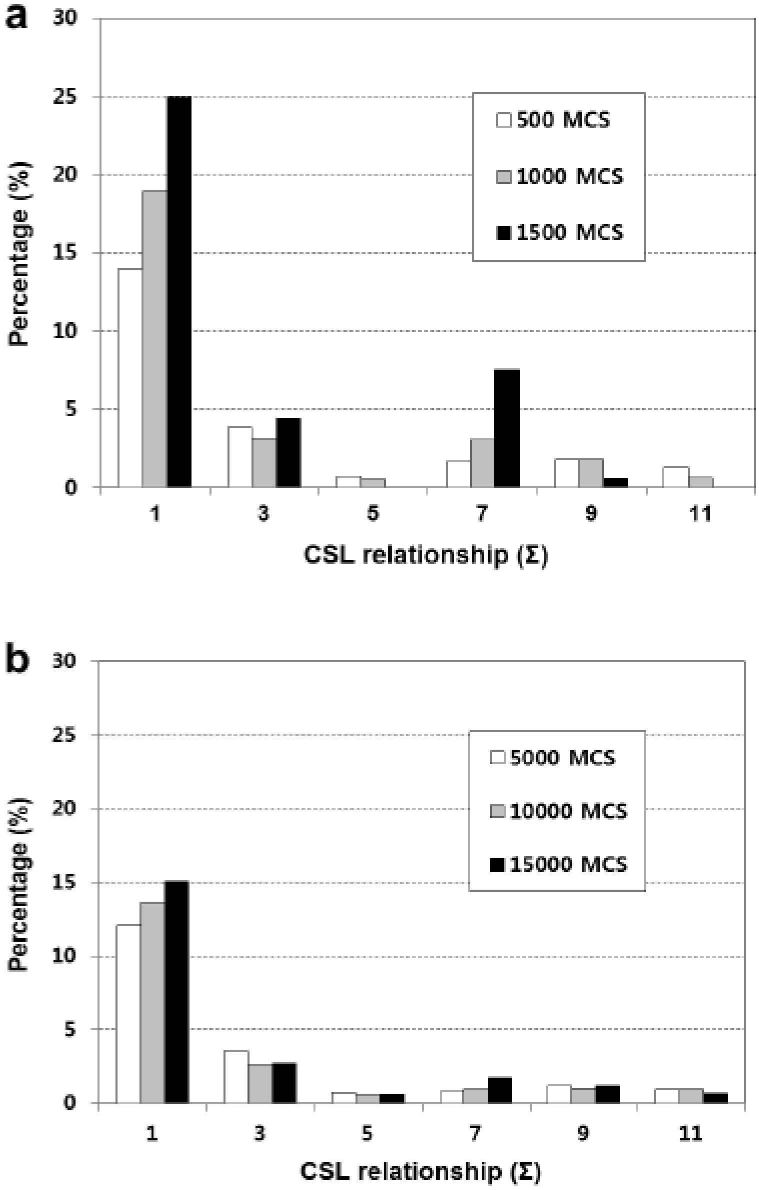

Figure 8.5 Distributions of low angle (Σ1) and CSL boundaries among the matrix grains during the grain growth for the cases (a) without and (b) with precipitates

8.3.2 Effect of sub-boundary on the abnormal grain growth

According to the mechanism of sub-boundary enhanced solid-state wetting, the presence of sub-boundaries inside Goss grains is responsible for their selective AGG [17, 21]. In order to examine the number of sub-boundaries on AGG, the MC simulation was performed with 0, 2, 4 and 8 sub-grains. To check whether the white Goss grain undergoes AGG or not, the condition of d(R/<R>)/dt > 0, which is generally used as a criterion for AGG, is examined. In Figure 8.6, R/<R>, which is the size ration of the white grain and the average matrix grains, is plotted against the simulation time for the white grains composed of 0, 2, 4 and 8 sub-grains. For the case without sub-grains, R/<R> increased initially but decreased after 7500 MCS. For the case with 2, 4 and 8 sub-grains, however, R/<R> continue to increase with simulation time and the growth rate of the white grain increases with increasing number of sub-grains. This result indicates that as the number of sub-grains increases, the AGG is enhanced.

Figure 8.7 shows the plot of R/<R> vs. simulation time for the sub-boundary energy of 0.05, 0.10, 0.15, 0.20 and 0.25 for the white Goss grain with 8 sub-grains. The overall slopes for the energy of 0.05, 0.10, 0.15 and 0.20 are positive, whereas the slope for 0.25 becomes negative after 10000 MCS. Therefore, as the sub-boundary energy increases, the effect of enhancing AGG is diminished. The sub-boundary energy of 0.25 in the present condition corresponds to the misorientation angle of ~1o. Experimentally, Park et al. [22] and Ushigami et al. [25] reported that the misorientation angles of sub-boundaries, which existed exclusively inside the abnormally-growing Goss grains, during secondary recrystallization in Fe-3%Si steel, were $0.15^o \sim 0.5^o$. Dorner et al. [26] also observed very low angle grain boundaries exclusively within primary recrystallized Goss grains. The exclusive existence of sub-boundaries in Goss grains, together with simulation results in Figures 8.6 and 8.7, supports the possibility that sub-boundaries should be responsible for selective AGG of Goss grains. These results indicate that AGG depends critically on the presence of sub-boundaries, implying that the correlation between crystallographic orientation, size and number of next neighbours of abnormally-growing grains is not critical to AGG in agreement with the report by Chen et al [67].

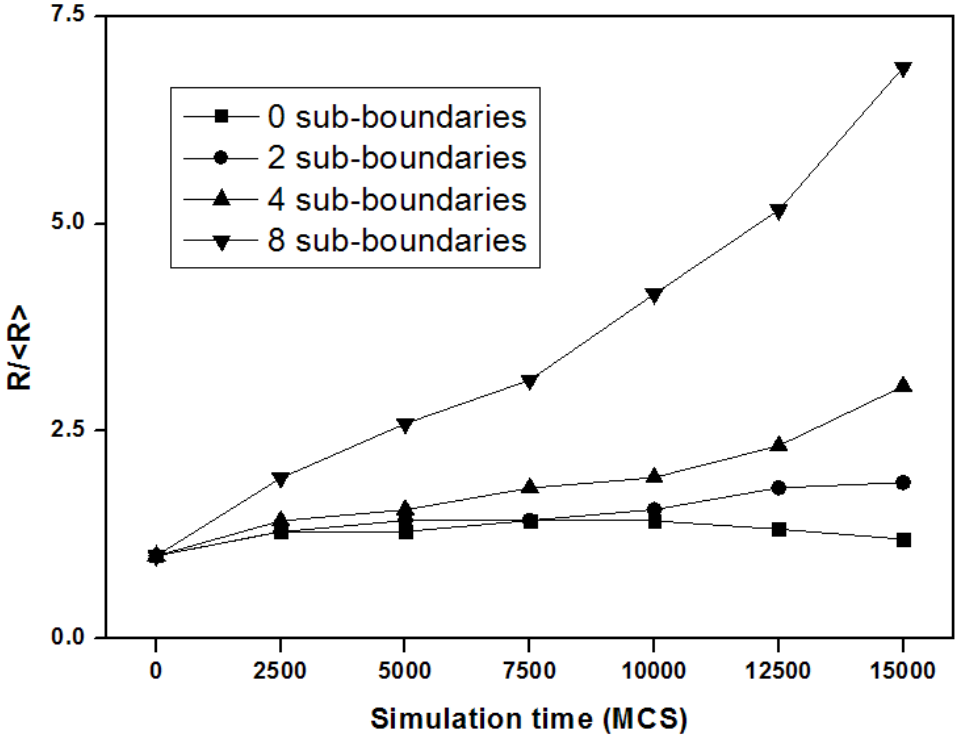

Figure 8.6 Plot of R/<R> vs. simulation time (MCS) of the white Goss grains with 0, 2, 4 and 8 sub-grains.

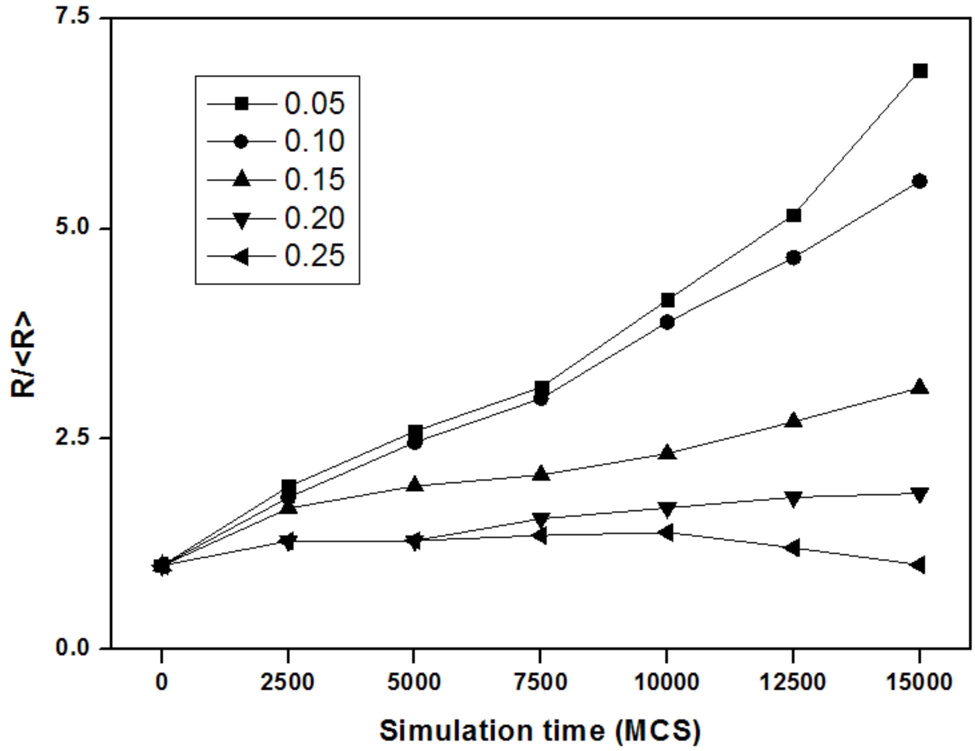

Figure 8.7 Plot of R/<R> vs. simulation time (MCS) of the white Goss grains of 8 sub-grains with various sub-boundary energy.

8.4 Comparisons between simulation and experimental results

8.4.1 Formation of island and peninsular grains

Numerous island and peninsular grains tend to be observed at or near the growth front of abnormally-growing grains, which is a unique feature of AGG. Based on EBSD measurements, Messina et al. [37] and Ko et al. [20] reported that island and peninsular grains tend to have low energy boundaries with abnormally-growing grains; they tend to have either low misorientation angles or CSL relationships. Based on the 3-D microstructure derived from successive images from sequential polishing and the observation, Ko et al. [20] suggested that island and peninsular grains are formed by solid-state wetting. Therefore, it is worth examining the possibility that our 3-D MC simulation, implementing the sub-boundary enhanced solid-state wetting in the presence of precipitates, can also reproduce island and peninsular grains. Since our initial simulation data are based on the real orientations obtained after primary recrystallization of Fe-3%Si steel, it is possible that island and peninsular grains might have a tendency to share a low energy boundary with the abnormally-growing grain like a real microstructure evolution. In order to check this possibility, the characteristics of grain boundaries between the abnormally-growing grain and island or peninsular grains were investigated in the simulation, which is then compared with experiments.

Figure 8.8(a) shows the microstructure evolution by the simulation at or near the growth front of an abnormally-growing white Goss grain, where island and peninsular grains are formed. Figure 8.8(b) shows the real microstructure of island and peninsular grains at or near the growth front of abnormally-growing Goss grains in Fe-3%Si steel. Misorientations between the abnormally-growing and island or peninsular grains in Figure 8.8(a) and (b) have it in common that they are low angles or have CSL relations as indicated in both figures.

To obtain statistically-reliable data, 154 and 220 island grains and 130 and 182 peninsular grains were examined in simulations and experiments, respectively. Figure 8.9(a) and b show percentages of low angle and CSL boundaries, respectively, for island and peninsular grains. The black and grey bars in Figure 8.9(a) and (b) indicate the percentages determined from experiments and MC simulations, respectively. In both experiments and simulations, about 35% of all grain boundaries of island and peninsular grains are low angle or CSL boundaries. Among them, $\Sigma 1$, which is low angle boundaries, is most dominant. These results indicate that MC simulations implementing the effects of sub-boundaries and precipitates reproduce realistic microstructures of numerous island and peninsular grains with ~ 35% of their boundaries having low energy.

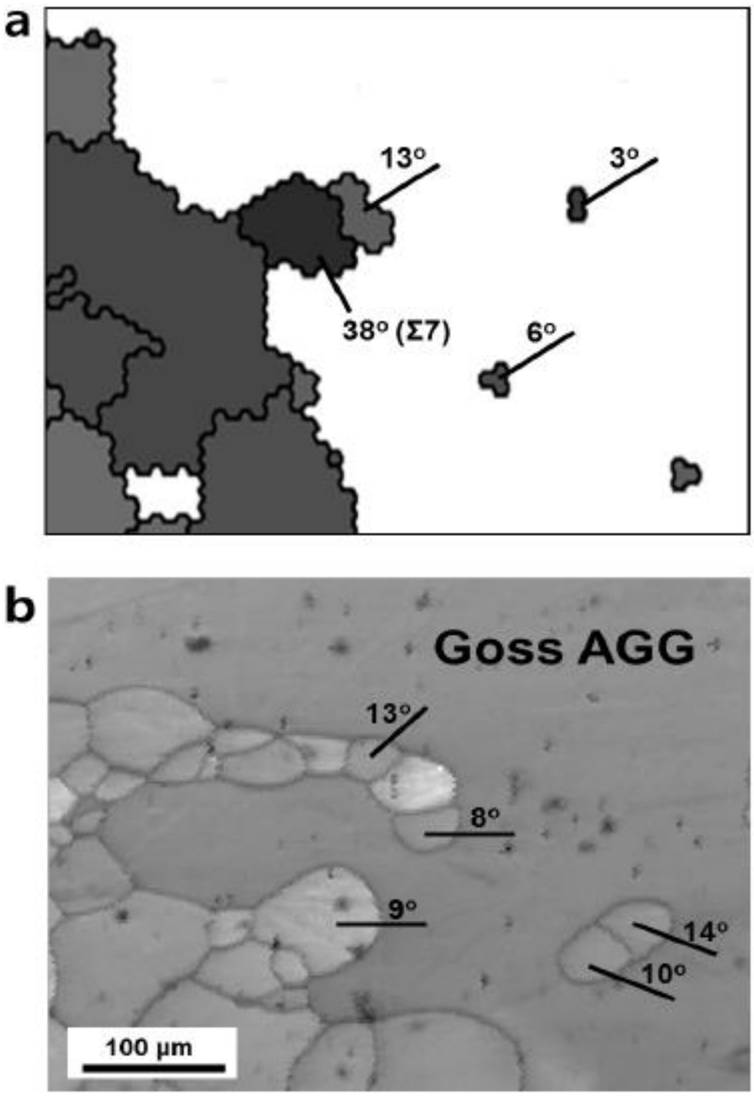

Figure 8.8 Microstructures near the growth front of abnormally-growing grains observed in (a) MC simulation and (b) Fe-3%Si steel. The numbers represent misorientations between the abnormally-growing and island or peninsula grains.

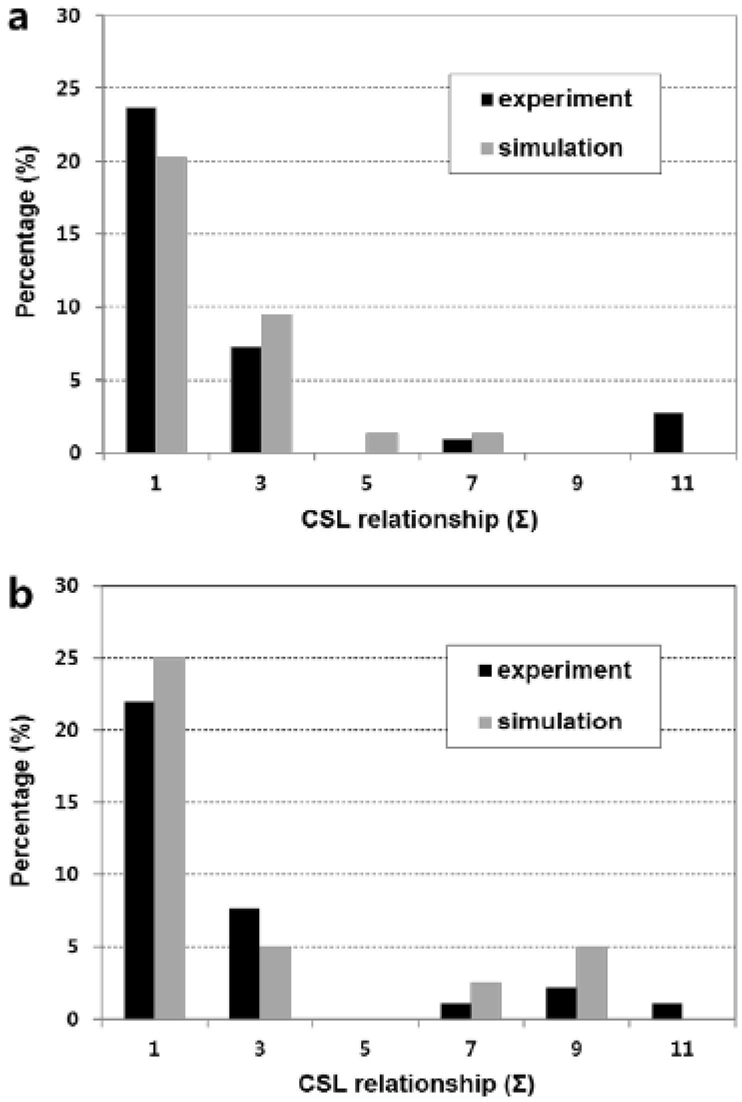

Figure 8.9 The distributions of CSL relationships between the abnormally-growing grains and two different types of grains; (a) island and (b) peninsular. The experiment and simulation results are represented by black and grey colors, respectively.

Compared with previous 3-D grain growth simulations either by MC [21] or by phase field model (PFM) [17] implementing the effect of sub-boundaries, the frequency of island and peninsular grains is much higher in the present 3-D MC simulations, which implement the effect of precipitates. If island or peninsular grains are formed by solid-state wetting in the absence of precipitates, those grains will disappear quickly because their grain boundaries, which are not imposed by the triple junction constraint, would migrate freely and fast. In the presence of precipitates, however, their migration would be inhibited, which would result in the high frequency of island or peninsular grains. This means that the frequency of island and peninsular grains would increase as the ratio of the wetting rate to the boundary migration rate increases.

On the other hand, in the present simulation the inherent mobility of low angle and CSL boundaries was not considered. In other words, the mobility of the grain boundaries is isotropic and assumed to be the same except the inhibition effect by precipitates. This assumption has an advantage in examining exclusively the effects of sub-boundaries and precipitates on AGG but has a disadvantage in that the microstructure evolution cannot be coupled with a real time scale. Monte Carlo simulations considering the mobility of grain boundaries were shown to produce the microstructure evolution coupled with a real time scale [69, 70].

One possibility that results from not considering the real grain boundary mobility would be the difference in the frequency of island and peninsular grains between simulations and experiments. Although the frequency depends on the experimental condition, our general observation is that the frequency is higher in experimental results than in the simulations. This difference might come from the low inherent mobility of low angle and CSL boundaries. This conclusion is in conflict with the previous suggestion that some CSL boundaries, especially Σ9, have higher mobility than general boundaries [8] [71]. But recently, we made ex-situ observations on the time evolution of numerous grains adjacent to abnormally-growing grains by sequential annealing of aluminium alloy (AA 5052). The observation reveals that CSL boundaries have lower mobility than general boundaries. And CSL boundaries such as Σ9 are observed at much higher frequency at or near the growth front of abnormally-growing grains not because they have high mobility but because they have low mobility.

8.4.2 Comparison with experimental results

Since the present simulation successfully reproduces the boundary characteristics of island and peninsular grains formed during AGG, it might reproduce other features of AGG. For example, Inokuti et al. [49] suggested a geometrical coalescence model as a mechanism of AGG based on his observation. They suggested that many primary grains with Goss orientation were formed near the steel surface, whose location corresponded to Goss areas having been formed by hot rolling; this was suggested as an inheritance mechanism by a structure memory. After Goss nuclei were independently formed and grown, an abnormal Goss grain is made by coalescence of the primary Goss nuclei as shown schematically in Figure 8.10.

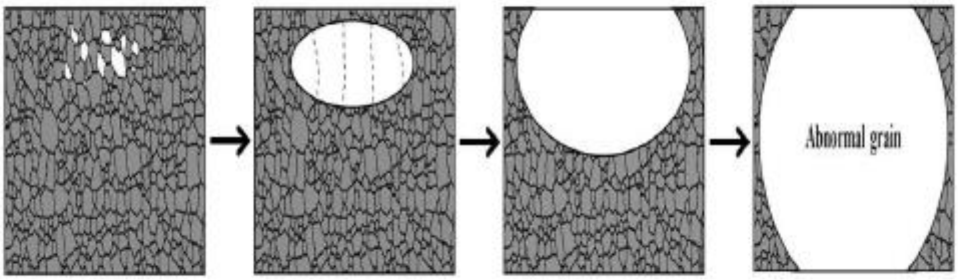

Figure 8.10 Schematics of the geometrical coalescence during secondary recrystallization of Fe-3%Si steel reported by Inokuti et al. [49]. Redrawn after ref [49].

This geometrical coalescence mechanism can be reinterpreted based on solid-state wetting. Goss nuclei, which appeared as separate grains and had been believed to form independently, are actually formed by solid-state wetting along triple junctions and originated from the identical grain. When a Goss grain grows by triple junction wetting, its 3-D shape can be highly irregular and even resemble an octopus. If an octopus is sliced through its legs and observed on a two-dimensional section, each leg appears separately but they are connected three dimensionally. Similarly, initial Goss nuclei, which may appear separate two dimensionally in Figure 10, are not actually separate but can be connected three dimensionally.

Homma and Hutchinson [10] and Ko et al. [50] observed this aspect by serial sectioning and observation of abnormally-growing grains at different depths below the sheet surface in Fe-3% Si steel. Figure 8.11(a) shows serial section images by EBSD near the growth front of an abnormally-growing Goss grain. Each EBSD image in Figure 8.11(a) was obtained after polishing the sample mechanically with about 10μm intervals with the Goss grain being represented by a white colour. Although the white grain inside the matrix grains appeared to be separated from the abnormally-growing white Goss grain in the first two images, they turned out to be the identical grain in the third image. It means that the two white Goss grains in the first two images of Figure 8.11(a) were actually the same grain connected three dimensionally.

This aspect can be observed in the MC simulation. Figure 8.11(b) shows the cross-section (x, y) images at z = 42, 43, 44 and 45 after 12000 MCS. The four white grains appear to be separated in the first image at z = 42. The two small white grains turned out to be the same grain and coalesced each other in the second image at z = 43. The other grain in the matrix coalesced with the abnormally-growing grain in the third image at z = 44. All four grains coalesced into one in the fourth image at z = 45. Therefore, the schematics shown in Figure 8.10, which became the basis for the geometrical coalescence model, can be regarded as an experimental evidence of the solid-state wetting mechanism.

Similarly, Park et al. [28] performed ex-situ observation of microstructure evolution during AGG in an aluminium alloy (AA 5052). Figure 8.12(a) shows the sequential microstructure evolution using EBSD during secondary recrystallization of the aluminium alloy. These images were obtained from the same area at accumulated annealing times of 15, 25, 30 and 40 min at 500^{o}C. An important point to notice here is that all white grains have the same orientation. From 15 to 40 min, all isolated white grains are merged and become a single abnormal grain.

This aspect of the sequential microstructure evolution could be reproduced by the MC simulation as shown in Figure 8.12(b). It shows cross-sections (x, y) images of a 3-D microstructure at z = 40 after 13000, 13300, 13600 and 14000 MCS. All white grains, which appeared separate initially, coalesced into an abnormally-growing grain for the time interval of 1000 MCS. Therefore, the coalescence of many primary grains in two-dimensions, which was observed by serial sectioning of abnormally-growing grains and by sequential annealing of the sample can also be regarded as an evidence of solid-state wetting.

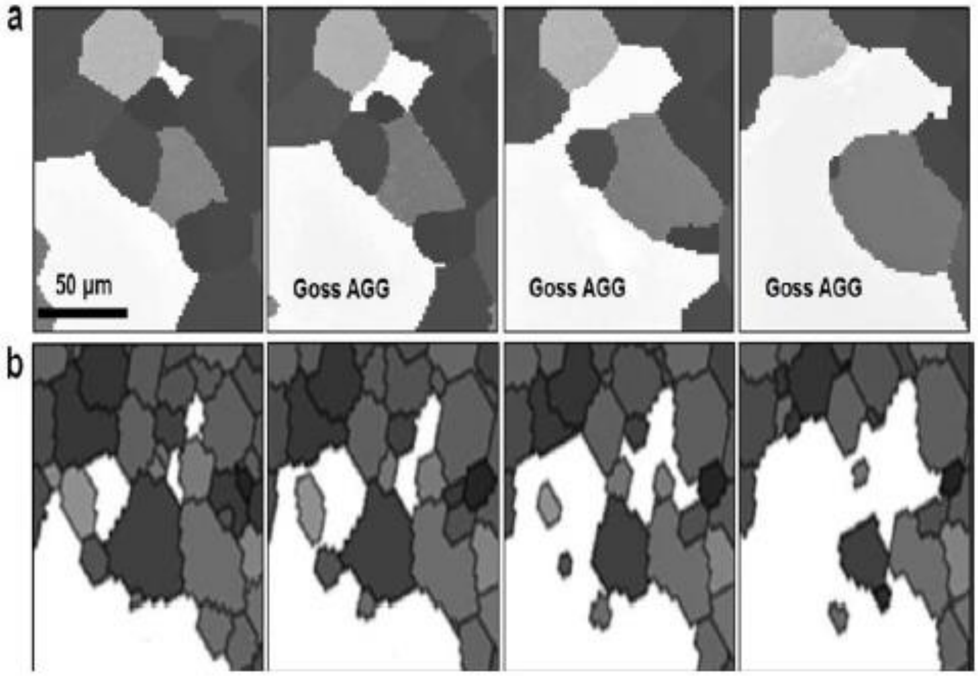

Figure 8.11 The serial sectioning images of abnormally-growing grains. (a) The microstructures of the Fe-3%Si steel successively polished with 10μm intervals and (b) the cross-sections of a 3-D simulation microstructure at z = 42, 43, 44 and 45 after 12000 MCS. The abnormally-growing grains are represented by white color.

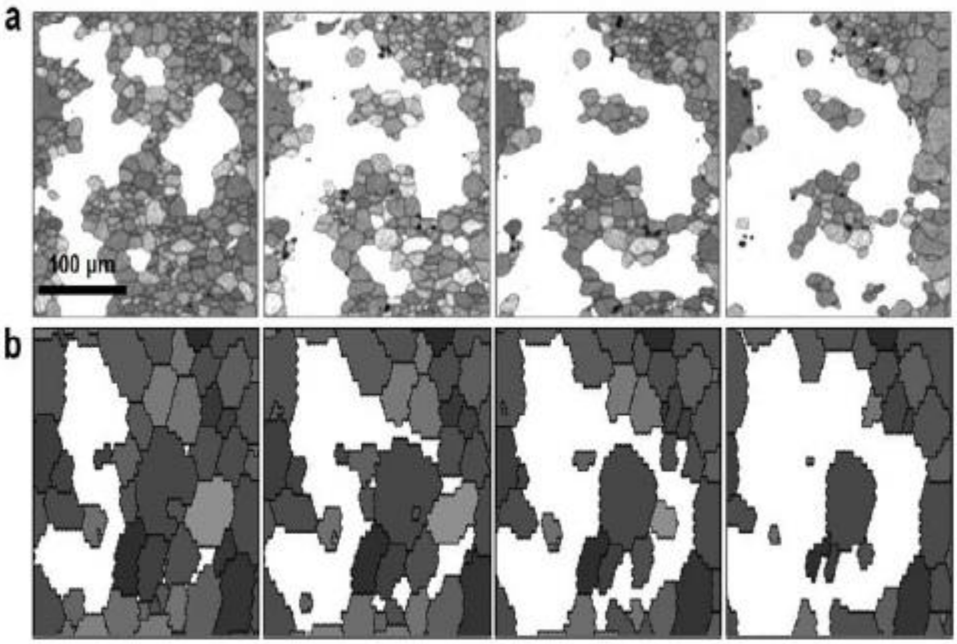

Figure 8.12 The time evolution of the microstructure during AGG observed in (a) an aluminum alloy for accumulated annealing times of 15, 25, 30 and 40 min at 500oC and (b) the cross-sections of a 3-D simulation microstructure at z = 40 after 13000, 13300, 13600 and 14000 MCS.

8.5 Three-dimensional morphologies of abnormally-growing Goss grains

In the above, the microstructure evolved by the simulation could reproduce many realistic features of abnormally-growing grains such as the formation of island and peninsular grains and the coalescence of abnormally-growing grains in two-dimensions. Another advantage of the simulation is that three-dimensional morphology of abnormally-growing grains can be structuralized as shown in Figure 8.13. Figure 8.13(a) and (c) shows cross-sections and Figure 8.13(b) and (d) shows three-dimensional morphologies of Goss grain growing by NGG and AGG, respectively. The shape of abnormally-growing grain (Figure 8.13(d)) is highly irregular and it has sharp wetting structures. This feature is a unique characteristic of abnormally-growing grain in comparison with normally-growing grain (Figure 8.13(b)). Therefore, it can be concluded that AGG occurs by triple-junction wetting.

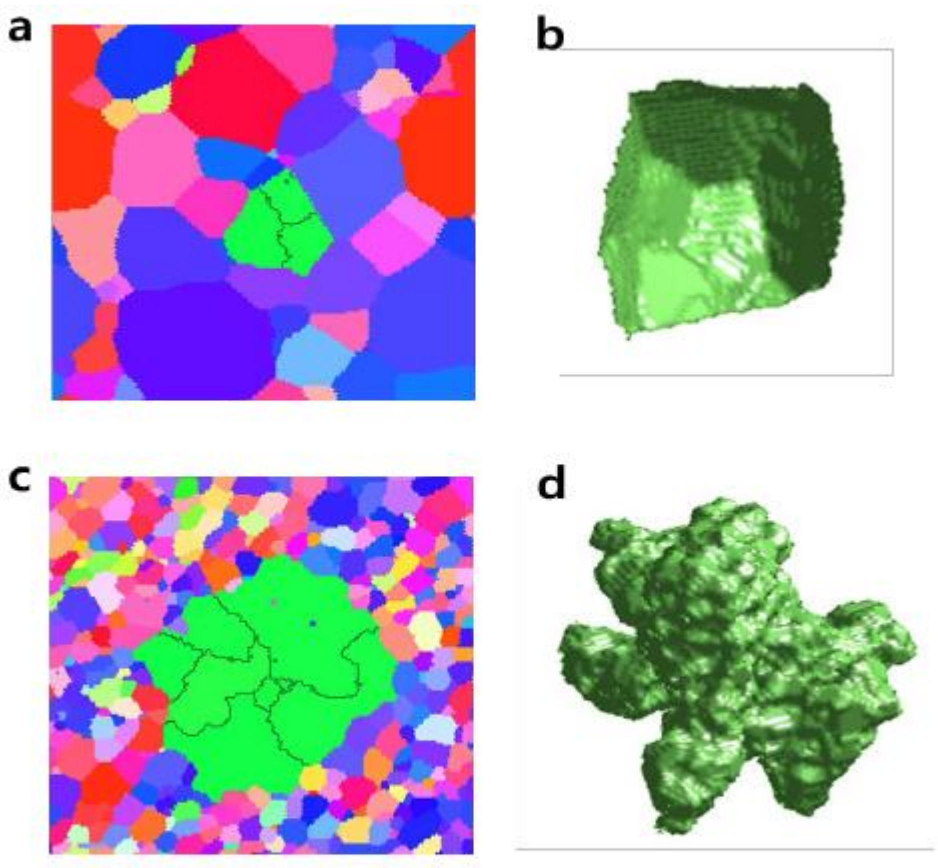

Figure 8.13 (a), (c) Two-dimensional microstructures of NGG and AGG and (b), (d) three-dimensional morphologies of Goss grain growing by NGG and AGG, respectively.

Reference

[1] M. Hillert, On the theory of normal and abnormal grain growth, Acta metallurgica 13 (1965) 227-238.

[2] J. Dennis, P. Bate, F. Humphreys, Abnormal grain growth in Al–3.5 Cu, Acta materialia 57 (2009) 4539-4547.

[3] J.B. Koo, D.Y. Yoon, Abnormal grain growth in bulk Cu—The dependence on initial grain size and annealing temperature, Metallurgical and Materials Transactions A 32 (2001) 1911-1926.

[4] S. Tsurekawa, T. Fukino, T. Matsuzaki, In-situ SEM/EBSD observation of abnormal grain growth in electrodeposited nanocrystalline nickel, International Journal of Materials Research 100 (2009) 800-805.

[5] S. Lee, D. Yoon, M. Henry, Abnormal grain growth and grain boundary faceting in a model Ni-base superalloy, Acta materialia 48 (2000) 3071-3080.

[6] R. Shimizu, J. Harase, Coincidence grain boundary and texture evolution in Fe-3% Si, Acta Metallurgica 37 (1989) 1241-1249.

[7] N.P. Goss, New development in electrical strip steels characterized by fine grain structure approaching the properties of a single crystal, Trans. Am. Soc. Met. 23 (1935) 511-531.

[8] J. Harase, R. Shimizu, D.J. Dingley, Texture evolution in the presence of precipitates in Fe−3% Si alloy, Acta Metall. Mater. 39 (1991) 763-770.

[9] Y. Ushigami, T. Kumano, T. Haratani, S. Nakamura, S. Takebayashi, T. Kubota, Secondary recrystallization in grain-oriented silicon steel, Mater. Sci. Forum 467 (2004) 853-862.

[10] H. Homma, B. Hutchinson, Orientation dependence of secondary recrystallisation in silicon-iron, Acta Mater. 51 (2003) 3795-3805.

[11] N. Rajmohan, J. Szpunar, Y. Hayakawa, A role of fractions of mobile grain boundaries in secondary recrystallization of Fe–Si steels, Acta Mater. 47 (1999) 2999-3008.

[12] A. Morawiec, Grain misorientations in theories of abnormal grain growth in silicon steel, Scr. Mater. 43 (2000) 275-278.

[13] A. Etter, T. Baudin, R. Penelle, Influence of the Goss grain environment during secondary recrystallisation of conventional grain oriented Fe–3% Si steels, Scr. Mater. 47 (2002) 725-730.
[14] G. Gottstein, Y. Ma, L. Shvindlerman, Triple junction motion and grain microstructure evolution, Acta Mater. 53 (2005) 1535-1544.
[15] G. Gottstein, L. Shvindlerman, B. Zhao, Thermodynamics and kinetics of grain boundary triple junctions in metals: Recent developments, Scr. Mater. 62 (2010) 914-917.
[16] N.-M. Hwang, Simulation of the effect of anisotropic grain boundary mobility and energy on abnormal grain growth, J. Mater. Sci. 33 (1998) 5625-5629.
[17] K.-J. Ko, P.-R. Cha, D. Srolovitz, N.-M. Hwang, Abnormal grain growth induced by sub-boundary-enhanced solid-state wetting: Analysis by phase-field model simulations, Acta Mater. 57 (2009) 838-845.
[18] D.-K. Lee, K.-J. Ko, B.-J. Lee, N.-M. Hwang, Monte Carlo simulations of abnormal grain growth by sub-boundary-enhanced solid-state wetting, Scr. Mater. 58 (2008) 683-686.
[19] D.-K. Lee, B.-J. Lee, K.-J. Ko, N.-M. Hwang, Comparison of the Advantages Conferred by Mobility and Energy of the Grain Boundary in Inducing Abnormal Grain Growth Using Monte Carlo Simulations, Mater. Trans. 50 (2009) 2521-2525.
[20] K.-J. Ko, P.-R. Cha, J.-T. Park, J.-K. Kim, N.-M. Hwang, Abnormal Grain Growth of Fe-3%Si Steel Approached by Solid-State Wetting Mechanism Adv. Mater. Res. 26-28 (2007) 65-68.
[21] K.-J. Ko, A.D. Rollett, N.-M. Hwang, Abnormal grain growth of Goss grains in Fe-3% Si steel driven by sub-boundary-enhanced solid-state wetting: Analysis by Monte Carlo simulation, Acta Mater. 58 (2010) 4414-4423.
[22] H.-K. Park, S.-D. Kim, S.-C. Park, J.-T. Park, N.-M. Hwang, Sub-boundaries in abnormally growing Goss grains in Fe-3% Si steel, Scr. Mater. 62 (2010) 376-378.
[23] H.-S. Shim, N.-M. Hwang, Secondary Recrystallization in Metals: Approach by Solid-State Wetting, Korean J. Met. Mater. 52 (2014) 663-687.
[24] C.-S. Park, T.-W. Na, J.-K. Kang, B.-J. Lee, C.-H. Han, N.-M. Hwang, Parallel

three-dimensional Monte Carlo simulations for effects of precipitates and sub-boundaries on abnormal grain growth of Goss grains in Fe–3% Si steel, Phil. Mag. 93 (2013) 4198-4212.

[25] Y. Ushigami, Y. Suga, N. Takahashi, K. Kawasaki, Y. Chikaura, H. Kii, Dynamic study of secondary recrystallization of 3% Si-Fe by synchrotron x-radiation topography, J. Mater. Eng. 13 (1991) 113-118.

[26] D. Dorner, L. Lahn, S. Zaefferer, Investigation of the primary recrystallisation microstructure of cold rolled and annealed Fe 3% Si single crystals with Goss orientation, Mater. Sci. Forum 467-470 (2004) 129-134.

[27] H.-S. Shim, T.-W. Na, J.-S. Chung, S.-B. Kwon, K. Gil, J.-T. Park, N.-M. Hwang, Synchrotron X-ray microdiffraction of Fe–3wt% Si steel focusing on sub-boundaries within Goss grains, Scr. Mater. 116 (2016) 71-75.

[28] H.-K. Park, H.-G. Kang, C.-S. Park, M.-Y. Huh, N.-M. Hwang, Ex situ observation of microstructure evolution during abnormal grain growth in aluminum alloy, Metall. Mater. Trans. 43 (2012) 5218-5223.

[29] H.-K. Park, S.-J. Kim, H.N. Han, C.-H. Han, N.-M. Hwang, Deformation Feature of Goss Grains in Fe-3% Si Steel Focused on Stored Energy after Cold Rolling, Materials transactions 51 (2010) 1547-1552.

[30] D. Srolovitz, G. Grest, M. Anderson, Computer simulation of grain growth—V. Abnormal grain growth, Acta Metall. Mater. 33 (1985) 2233-2247.

[31] C.-S. Park, T.-W. Na, H.-K. Park, D.-K. Kim, C.-H. Han, N.-M. Hwang, Misorientation characteristics of penetrating morphologies at the growth front of abnormally growing grains in aluminum alloy, Phil. Mag. Lett. 92 (2012) 344-351.

[32] H. Park, D.-Y. Kim, N.-M. Hwang, Y.-C. Joo, C.-H. Han, J.-K. Kim, Microstructural evidence of abnormal grain growth by solid-state wetting in Fe-3% Si steel, J Appl Phys 95 (2004) 5515-5521.

[33] W.T. Read, W. Shockley, Dislocation Models of Crystal Grain Boundaries, Phys Rev 78 (1950) 275-289.

[34] D.G. Brandon, The structure of high-angle grain boundaries, Acta Metall. 14 (1966) 1479-1484.

[35] H.-K. Kim, W.-S. Ko, H.-J. Lee, S.-G. Kim, B.-J. Lee, An identification scheme of grain boundaries and construction of a grain boundary energy database, Scr. Mater. 64 (2011) 1152-1155.
[36] B.-J. Lee, S.-H. Choi, Computation of grain boundary energies, Modelling Simul. Mater. Sci. Eng. 12 (2004) 621-632.
[37] R. Messina, M. Soucail, T. Baudin, L.P. Kubin, Observations of and model for insular grains and grain clusters formed during anomalous grain growth in N18 superalloy, J Appl Phys 84 (1998) 6366-6371.
[38] N. Maazi, N. Rouag, A. Etter, R. Penelle, T. Baudin, Influence of neighbourhood on abnormal Goss grain growth in Fe–3% Si steels: Formation of island grains in the large growing grain, Scr. Mater. 55 (2006) 641-644.
[39] S.-B. Lee, N.-M. Hwang, C.-H. Han, D.-Y. Yoon, Formation of islands and peninsulas of fine grains during the secondary recrystallization of an Fe-3wt% Si steel, Scr. Mater. 39 (1998) 825-829.
[40] J. Konrad, S. Zaefferer, D. Raabe, Investigation of orientation gradients around a hard Laves particle in a warm-rolled Fe 3 Al-based alloy using a 3D EBSD-FIB technique, Acta Materialia 54 (2006) 1369-1380.
[41] W. Xu, M. Ferry, N. Mateescu, J. Cairney, F. Humphreys, Techniques for generating 3-D EBSD microstructures by FIB tomography, Materials characterization 58 (2007) 961-967.
[42] W.-G. Lu, C.-Y. Su, T.-B. Lu, L. Jiang, J.-M. Chen, Two stable 3D metal-organic frameworks constructed by nanoscale cages via sharing the single-layer walls, Journal of the American Chemical Society 128 (2006) 34-35.
[43] E. Maire, P. Colombo, J. Adrien, L. Babout, L. Biasetto, Characterization of the morphology of cellular ceramics by 3D image processing of X-ray tomography, Journal of the European Ceramic Society 27 (2007) 1973-1981.
[44] D. Srolovitz, M.P. Anderson, P.S. Sahni, G.S. Grest, Computer simulation of grain growth—II. Grain size distribution, topology, and local dynamics, Acta metallurgica 32 (1984) 793-802.
[45] G. Grest, D. Srolovitz, M. Anderson, Computer simulation of grain growth—IV. Anisotropic grain boundary energies, Acta Metallurgica 33 (1985) 509-520.

[46] A. Rollett, D. Srolovitz, M. Anderson, Simulation and theory of abnormal grain growth—anisotropic grain boundary energies and mobilities, Acta metallurgica 37 (1989) 1227-1240.
[47] S.G. Kim, Y.B. Park, Grain boundary segregation, solute drag and abnormal grain growth, Acta Materialia 56 (2008) 3739-3753.
[48] A. Momose, W. Yashiro, S. Harasse, H. Kuwabara, Four-dimensional X-ray phase tomography with Talbot interferometry and white synchrotron radiation: dynamic observation of a living worm, Optics express 19 (2011) 8423-8432.
[49] Y. Inokuti, C. Maeda, Y. Ito, Computer Color Mapping of Configuration of Goss Grains after an Intermediate Annealing in Grain Oriented Silicon Steel, Transactions of the Iron and Steel Institute of Japan 27 (1987) 139-144.
[50] K.-J. Ko, J.-T. Park, J.-K. Kim, N.-M. Hwang, Morphological evidence that Goss abnormally growing grains grow by triple junction wetting during secondary recrystallization of Fe-3% Si steel, Scripta Materialia 59 (2008) 764-767.
[51] C.-S. Park, H.-K. Park, H.-S. Shim, T.-W. Na, C.-H. Han, N.-M. Hwang, New understanding of the role of coincidence site lattice boundaries in abnormal grain growth of aluminium alloy, Phil. Mag. Lett. 95 (2015) 220-228.
[52] Y. Inokuti, C. Maeda, Y. Ito, Formation of the Goss Texture in Grain Oriented Silicon Steel Containing a Small Amount of Molybdenum, Tetsu-to-Hagane(J. Iron Steel Inst. Jpn.) 70 (1984) 2057-2064.
[53] T. Sakai, M. Matsuo, M. Tanino, T. Shindo, M. Shiozaki, Secondary recrystallization process of high permeability grain oriented silicon steel. ICOTOM, vol. 6, 1981. p.938-947.
[54] M. Matsuo, T. Sakai, Y. Suga, Origin and development of through-the-thickness variations of texture in the processing of grain-oriented silicon steel, Metallurgical Transactions A 17 (1986) 1313-1322.
[55] H.-K. Park, J.-H. Kang, C.-S. Park, C.-H. Han, N.-M. Hwang, Pancake-shaped growth of abnormally-growing Goss grains in Fe–3% Si steel approached by solid-state wetting, Materials Science and Engineering: A 528 (2011) 3228-3231.
[56] S. Mishra, C. Därmann, K. Lücke, On the development of the Goss texture in

iron-3% silicon, Acta Metallurgica 32 (1984) 2185-2201.
[57] D. Raabe, Z. Zhao, S.-J. Park, F. Roters, Theory of orientation gradients in plastically strained crystals, Acta Materialia 50 (2002) 421-440.
[58] S.H. Lee, D.N. Lee, Analysis of deformation textures of asymmetrically rolled steel sheets, International journal of mechanical sciences 43 (2001) 1997-2015.
[59] C. Esling, H. Bunge, J. Muller, Description of the texture by distribution functions on the space of orthogonal transformations. Implications on the inversion centre, Journal de Physique Lettres 41 (1980) 543-545.
[60] V.Y. Novikov, Secondary recrystallization evolution and pinning force behaviour, Scripta Materialia 37 (1997) 463-469.
[61] R. Messina, M. Soucail, L. Kubin, Monte Carlo simulation of abnormal grain growth in two dimensions, Materials Science and Engineering A 308 (2001) 258-267.
[62] M. Anderson, G. Grest, R. Doherty, K. Li, D. Srolovitz, Inhibition of grain growth by second phase particles: three dimensional Monte Carlo computer simulations, Scripta metallurgica 23 (1989) 753-758.
[63] C.-S. Park, T.-W. Na, H.-K. Park, B.-J. Lee, C.-H. Han, N.-M. Hwang, Three-dimensional Monte Carlo simulation for the effect of precipitates and sub-boundaries on abnormal grain growth, Scripta Materialia 66 (2012) 398-401.
[64] U.F. Kocks, C.N. Tomé, H.R. Wenk. Texture and Anisotropy, University PressCambridge, 1998.
[65] D. Solas, P. Gerber, T. Baudin, R. Penelle, Monte Carlo method for simulating grain growth in 3 D Influence of lattice site arrangements. Materials Science Forum, vol. 467-470, 2004. p.1117-1122.
[66] L. Dagum, R. Menon, OpenMP: An industry standard API for shared-memory programming, Ieee Comput Sci Eng 5 (1998) 46-55.
[67] N. Chen, S. Zaefferer, L. Lahn, K. Günther, D. Raabe, Effects of topology on abnormal grain growth in silicon steel, Acta Materialia 51 (2003) 1755-1765.
[68] N.-M. Hwang, B.-J. Lee, C.-H. Han, Texture evolution by grain growth under a system of anisotropic grain boundary energy, Scripta Materialia 37 (1997) 1761-1767.

[69] D. Raabe, Scaling Monte Carlo kinetics of the potts model using rate theory, Acta Materialia 48 (2000) 1617-1628.
[70] A.D. Rollett, D. Raabe, A hybrid model for mesoscopic simulation of recrystallization, Computational Materials Science 21 (2001) 69-78.
[71] P. Lin, G. Palumbo, J. Harase, K. Aust, Coincidence site lattice (CSL) grain boundaries and Goss texture development in Fe-3% Si alloy, Acta materialia 44 (1996) 4677-4683.

요약(국문초록)

비정상 입자 성장은 특정 입자가 다른 입자에 비해 비정상적으로 빠르게 성장하는 현상으로 많은 금속계에서 보고되었다. 특히, Fe-3%Si steel에서의 비정상 입자 성장은 방향성 전기강판의 생산에 이용되어 관련한 많은 연구가 진행되었다. 하지만 많은 연구에도 불구하고 비정상 입자 성장의 정확한 원리가 규명되지 않고 있다.

이런 비정상 입자 성장을 설명하기 위해 제시된 이론이 바로 아경계에 의한 고상 젖음 이론이다. 이 이론은 입자 성장의 속도 결정 단계가 결정입계 삼중 접합선 혹은 사중 접합점의 이동이라고 여기고 이 삼중 접합선 혹은 사중 접합점이 빠르게 움직이기 위해서는 젖음이 일어나야 된다고 설명하고 있다. 이 이론에 따르면 이런 젖음이 일어날 확률을 아경계가 높여주어 비정상 입자 성장이 일어난다고 설명하고 있다.

우선 알루미늄 합금 5052에서 고상 젖음이 일어나는지를 확인하기 위하여 고상 젖음이 일어날 때 생길 수 있는 형상을 EBSD 장비를 이용하여 조사하고 이

형상에 대해 입계에서의 결정 방위 차이각을 이용해 입계의 에너지를 예측해 보았다. 고상 젖음이 일어났을 때 생길 수 있는 2차원적인 형상은 젖음 방향과 평행한 평면에서 본 경우와 젖음 방향과 수직한 평면에서 본 경우로 나눌 수 있다. 젖음 방향과 평행한 평면에서 본 경우 비정상 성장 중인 입자가 만들어내는 두 입계가 다른 두 입자가 만들어내는 입계를 젖어 들어가는 형태를 보인다. 이 때 아경계에 의한 비정상 입자 성장이론을 이용하면 젖음 현상이 일어나기 위한 조건을 구할 수 있고 계산을 통해 이 조건을 만족하고 고상 젖음이 일어날 수 있음을 간접적으로 증명하였다. 또 젖음 방향과 수직한 면에서 본 경우 비정상 성장 중인 입자에서 떨어진 입자가 비정상 성장 중인 입자와 동일한 방위를 갖는 것을 확인할 수 있었고 연속적인 연마를 통해 이 입자가 비정상 성장 중인 입자와 연결되어 있음을 확인할 수 있었다. 이런 결과들을 통해 알루미늄 합금 5052에서의 비정상 입자 성장이 고상 젖음에 의해 일어나는 것을 간접적으로 확인하였다.

또, 비정상 입자 성장을 정확히 이해하기 위해서 비정상 입자 성장의 입체적인 형태를 삼차원 몬테카를로 전산 모사를 통해 예측하였다. 전산 모사는 아경계와 석출물 그리고 실제 방위를 이용하여 구현하였다. 전산 모사에 의하면 비

정상 입자 성장이 아경계와 석출물이 동시에 존재할 때 일어나고 이를 통해 비정상 입자 성장이 아경게에 의한 고상 젖음 현상에 의해 일어날 수 있다는 것을 확인할 수 있다. 실제 비정상 성장 중인 입자의 입체적인 형태를 확인하기 위해서 순차적인 연마를 통해 여러 장의 평면적인 형상을 얻었고 이를 삼차원으로 재구축하였다. 전산 모사에 의한 입자의 형태와 순차적인 연마를 통해 재구축된 입자의 형태가 매우 흡사하였다. 이 둘은 모두 섬 혹은 반도형태의 입자들이 확인되었고 매우 복잡한 형태의 입계를 갖고 있다. 이런 유사성은 본 전산모사가 현실을 매우 잘 반영하고 있다는 것을 의미하고 이 전산모사를 통하여 집합조직과 아경계의 에너지에 따라 어떻게 비정상 입자 성장의 거동이 달라지는지를 확인하였다.

본 분석에 따르면 비정상 입자 성장의 속도는 집합조직에 의해 결정된다. 비대칭 압연을 통하여 이런 집합조직을 제어할 수 있고 이렇게 제어된 집합조직은 방향성 전기강판의 전자기적 성질을 높이는데 이용될 수 있다.

주요어(主要語): 비정상 입자 성장; 고상 젖음; 아경계; 입계 에너지; 삼차원 형상; 몬테카를로 전산모사; 연속적인 연마; 비대칭 압연

학 번: 2010-20599